International Journal of Thermofluids 24 (2024) 100936

Contents lists available at ScienceDirect

International Journal of Thermofluids

journal homepage: www.sciencedirect.com/journal/international-journal-of-thermofluids

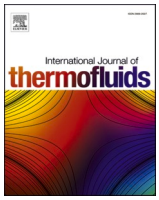

Synergistic effects of magnetic fields and Y-obstacles on a nanofluid-based split lid-driven thermal system

Anurag Kabiraj [a], Nirmalendu Biswas [b,*], Nirmal K. Manna [a], Dipak Kumar Mandal [c], Ali J. Chamkha [d]

[a] Department of Mechanical Engineering, Jadavpur University, Kolkata 700032, India
[b] Department of Power Engineering, Jadavpur University, Kolkata 700106, India
[c] Department of Mechanical Engineering, Government Engineering College, Samastipur, Bihar-848127, India
[d] Faculty of Engineering, Kuwait College of Science and Technology, Doha District, Kuwait

ARTICLE INFO

Keywords:
Y-shaped obstacle
Mixed convection
Nanofluid
Magnetohydrodynamics (mhd)
Heat transfer
Entropy generation

ABSTRACT

This study investigates the complex hydrothermal behavior in a novel split-driven square cavity filled with CuO-water nanofluid and featuring a Y-shaped obstacle. The research explores the interplay among mixed convection, magnetohydrodynamics (MHD), and geometric factors in a previously unexamined configuration. The upper wall is split into two isothermally heated, translating sections, while the bottom wall and Y-shaped obstacle provide cooling boundaries. Using finite element analysis, we examine the effects of Reynolds number (Re = 10–200), Rayleigh number (Ra = 10^3–10^6), Hartmann number (Ha = 0–70), and magnetic field inclination (λ = 0–150°) on flow patterns, heat transfer, and entropy generation. Energy flux vectors are utilized to analyze thermal energy transport dynamics. Key findings are as follows. (1) Increasing Re enhances fluid mixing, resulting in up to a 65 % increase in the average Nusselt number (Nu). (2) Nu peaks at Ra ≈ 10^5, then slightly decreases due to complex force interactions. (3) Increasing Ha suppresses convection, reducing Nu by up to 30 %. (4) Optimal heat transfer occurs at λ ≈ 75° (5) The Y-shaped obstacle enhances heat transfer by up to 30 %. These results provide insights for optimizing thermal management in applications requiring precise temperature control, potentially improving energy efficiency in advanced heat transfer systems.

1. Introduction

Convection is a fundamental method of heat transfer, relying on the movement of a fluid—either gas or liquid—which carries energy within its mass, facilitating heat transfer or interaction. When convection is enhanced by an external force, such as the movement introduced by a fan or shear-driven flow from a lid-driven system, it is referred to as forced convection. In contrast, when the fluid motion is driven by its own buoyancy due to factors like temperature, density, and compressibility, it is known as natural or free convection. This convective process plays a pivotal role in numerous engineering and scientific applications. However, since free convection alone is often inefficient, a combination of both free and forced convection is typically more effective in thermal systems that require precise temperature control, such as electronic devices, medical equipment, and metal casting processes.

In this context, the lid-driven cavity problem serves as a fundamental issue in thermal and fluid sciences, especially for engineers. It acts as a key example for analyzing flow patterns and velocity distributions while developing numerical techniques to address complex challenges. The theoretical and mathematical groundwork for this problem can be traced to the pioneering research of Bruneau et al. [1], who conducted a detailed examination of flow conditions across different Reynolds numbers.

The classical problem of natural convection within a square cavity has been extensively covered in the important work of de Vahl Davis [2]. This research provides a thorough explanation of the computational methods and solution approaches, along with detailed insights into the underlying physics, flow visualization, and isotherm distribution. Scenarios involving the simultaneous interaction of fluid flow, heat transfer, and other physical phenomena are critical across various applications such as electronic cooling systems, refrigeration, aerospace, aviation, and hydraulics. Achieving accurate results requires meticulous modeling and analysis.

One effective method is conjugate heating, which integrates both conduction and convection by introducing an obstruction within the

* Corresponding author at: Department of Power Engineering, Jadavpur University, Salt Lake City, Kolkata 700106, India.
E-mail address: biswas.nirmalendu@gmail.com (N. Biswas).

https://doi.org/10.1016/j.ijft.2024.100936

Available online 30 October 2024

Nomenclature

Acronyms

B	intensity of magnetic field (N A^{-1} m^{-2})
Ec	Eckert number
g	gravity (m s^{-2})
H	length scale (m)
Ha	Hartmann number
k	thermal conductivity ($Wm^{-1}K^{-1}$)
NS	dimensionless entropy generation
Nu	average Nusselt number
P	dimensionless pressure
Pr	Prandtl number
Ra	Rayleigh number
Re	Reynolds number
T	temperature (K)
u, v	components velocities (m s^{-1})
U, V	components velocities (dimensionless)
x, y	Cartesian coordinates (m)
X, Y	dimensionless Cartesian coordinates

Greek symbols

α	thermal diffusivity (m^2 s^{-1})
β	thermal expansion constant (K^{-1})
θ	temperature (dimensionless)
λ	angle for the magnetic field
μ	dynamic viscosity (kg $m^{-1}s^{-1}$)
ν	kinematic viscosity (m^2 s^{-1})
ρ	density (kg m^{-3})
σ	electrical conductivity (Sm^{-1})
φ	nanoparticles volume fraction
ψ	nondimensional stream function
Π	nondimensional heat function

Subscripts

a	ambient
c	cold
f	base fluid
gen	generation
h	hot
loc	local
m	magnetic
max	maximum
r	property ratio
s	solid nanoparticles
th	thermal
tot	total
v	viscous

flow domain. Research by Das et al. [3] provides valuable insights into how the average Nusselt number—a key indicator of heat transfer rate—varies with changes in cavity inclination and Rayleigh number, considering different ratios of solid-to-fluid thermal conductivity. Their work offers a solid basis for further research in this area. Aminossadati et al. [4] investigated the impact of using a smart fluid, specifically a nanofluid, within the flow domain. They employed an Ethylene-Glycol-Copper nanofluid and observed improved heat transfer rates under certain conditions. Merrikh et al. [5] examined how variations in the average Nusselt number affected heat transfer rates by analyzing different conditions, including the solid-to-fluid thermal conductivity ratio, Rayleigh number, and the number of embedded (disconnected) blocks in the flow domain. Importantly, they maintained a constant volume fraction while varying the number of square blocks, ensuring that the total solid mass remained unchanged. Hu et al. [6] explored the problem of conjugate natural convection with various morphological obstructions, continuing the work of previous studies. They analyzed two types of geometries: one with rectangular structures attached to adiabatic walls (fins) and another with disconnected square blocks. Their comprehensive research serves as a valuable reference for further studies in this area.

Moving beyond square enclosures, the effects of different enclosure shapes and configurations are also worth examining. For example, Mohebbi et al. [7] investigated the implications of using an L-shaped cavity in their analysis, highlighting how variations in study parameters influence the results. Khan et al. [8] and Islam et al. [9] both studied mixed convection in a lid-driven cavity with a square obstacle. Khan et al. focused on a cavity with a heated bottom wall and cooled sidewalls, examining the effects of Reynolds number, Grashof number, and Prandtl number on heat transport. In contrast, Islam et al. analyzed an isothermal (cooled) cavity containing a heated block, exploring how changes in the size and position of the block affect heat transfer. Boulahia et al. [10] looked into the effects of placing a cold rectangular obstacle, akin to a fin, connected to the bottom wall. They varied the fin height to study its impact on the Nusselt number and its relation to the Rayleigh number. Fins are structural extensions, typically rectangular or cylindrical in shape, that protrude from the surfaces of heat-generating components. These structures are specifically designed to increase the surface area available for heat dissipation, thereby enhancing the overall cooling efficiency of the system. Commonly found on electric motors, internal combustion engines, and similar devices, these fins help to prevent overheating by improving heat transfer to the surroundings.

In the presence of a magnetic field, the magnetic field interacts with the fluid within the flow domain and associated convection is termed magnetohydrodynamics (MHD). In this phenomenon, as the electrically conductive fluid moves through the cavity, a Lorentz force is generated, which can either dampen or accelerate the flow depending on the conditions. Bourantas et al. [11] investigated MHD natural convection in a square enclosure filled with a micropolar nanofluid. Their study revealed how variations in parameters such as the Rayleigh number, Hartmann number, and nanoparticle volume fraction affected the average Nusselt number. Javed et al. [12] examined MHD natural convection in a square enclosure with vertical adiabatic walls, where the top wall is cold, the bottom wall is hot, and a heated obstacle is included. In their study, the cavity, containing a ferrofluid and subjected to a magnetic field perpendicular to the sidewalls, showed a reduction in circulation strength due to the Hartmann number, although increasing the Rayleigh number led to an improvement in heat transfer rates. Additionally, Javed et al. [13] explored the effects of MHD combined with mixed convection, shedding light on how changes in various non-dimensional numbers and parameters impact the flow and heat transfer characteristics.

Ali et al. [14], Hussein et al. [15], and Parvin et al. [16] conducted simulations to explore MHD natural convection under various conditions. Ali et al. investigated a differentially heated cavity featuring a tilted obstacle. Hussein et al. examined a scenario with an adiabatic block within an enclosure that combines Dirichlet and Neumann boundary conditions. Parvin et al. focused on a heated obstacle with a circular cross-section inside a cavity, where one wall was cold and the rest were adiabatic. Usman et al. [17] incorporated both natural convection and radiation effects in their study, analyzing heat transfer in a cavity with a hot top wall and cold remaining walls, which contained both hot and cold obstacles. Ashouri et al. [18] performed a detailed analysis of MHD natural convection in a square cavity with embedded solid blocks. They varied the Rayleigh number, Hartmann number, solid-to-fluid thermal conductivity ratio, and the number of solid blocks

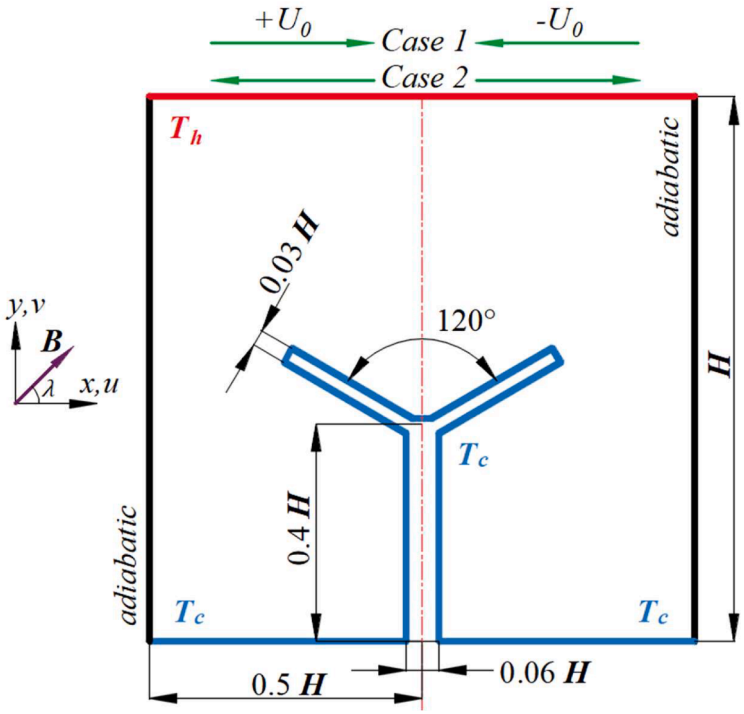

Fig. 1. Schematic of the problem geometry along with boundary conditions.

(while keeping the volume fraction constant) to examine their effects on local and average Nusselt numbers, thereby measuring heat transfer rates. Notably relevant to our research is Khan et al. [19], which explores MHD mixed convection within a split lid-driven cavity with a Y-shaped obstruction. Additional details can be found in references [20–27].

All these studies have emphasized the importance of mixed convective phenomena for improving heat transfer. However, fundamental aspects of a split-driven cavity comprising a nanofluid, oriented magnetic field in the presence of complex-shaped obstruction are still underexplored. Therefore, the present study seeks to close these research gaps by examining the complex hydrothermal behavior inside a split-driven cavity filled with nanofluid and subjected to oriented magnetic fields. In particular, we investigate a novel enclosure filled with CuO (copper oxide)-water nanofluid and featuring a Y-shaped obstacle. The upper wall is split into two parts heated isothermally and translating, while the bottom wall and Y-shaped obstacle provide the cooling boundaries. This work is novel because it examines the combined effects in detail, which has never been done before in this particular combination. Therefore the innovative goals of this study are:

- The combination of intriguing features includes split wall translation, moving heated surfaces, Y-shaped cold stationary obstruction, oriented magnetic fields, and nanofluids.
- A comprehensive analysis of the impacts of important dimensionless parameters, such as the direction of the hot moving walls, speed of the wall motions (Re), buoyancy strength (Ra), magnetic intensity (Ha), and magnetic field angle (λ).
- The dynamics of the thermal energy transport process are analyzed utilizing the energy flux vectors tool, which helps to clarify the physical processes that underlie the change in heat energy transport patterns, under various parametric influences.
- Determining the ideal configuration of operational and geometric characteristics to maximize heat transfer enhancement and minimize the total irreversibility generation.

To achieve these goals, a thorough numerical parametric analysis is carried out to investigate the impacts of all the control variables as mentioned above. The findings of this investigation have significant ramifications for how effective heat transfer systems are designed and managed under complex scenarios. Furthermore, by gaining new insights, manufacturing processes that need precise temperature control and energy storage systems may be improved, potentially resulting in lower energy consumption and higher system efficiency. Therefore, this research adds significant insights to the field of thermal management for the next generation of high-performance thermal management systems.

2. Problem statement mathematical modeling

The geometry in this study consists of a square cavity (side length H) with a Y-shaped obstruction extending from the bottom. The axis of the Y-shaped obstacle is bilaterally symmetric and is strategically positioned along the mid-plane of the cavity. The trunk of the Y obstacle has a thickness of $0.06H$, while the thickness of the wings measures $0.03H$, with the included angle between the wings set at 120° The intersection point of the internal sides of the wings occurs at a height of $0.4H$ from the base, and the wings are joined by a line at a height of $0.01H$ from this virtual point (as it lies within the geometry), thereby completing the model. An extensive diagram illustrating the dimensions and structure is presented in Fig. 1. The upper wall of the cavity is divided into two sections (each of length $0.5H$), heated isothermally at temperature T_h and moving at a uniform velocity U_0. The bottom wall and the Y-shaped obstacle act as cooling boundaries at temperature T_c [28,29]. The study is conducted for two scenarios: Case 1 (inward translation) with $U_l = +1$ and $U_r = -1$, and Case 2 (outward translation) with $U_l = -1$ and $U_r = +1$. A magnetic field (strength B) is applied over the entire flow domain at an angle of λ as shown in Fig. 1.

The cavity is filled with nanofluid (mono nanofluid, a single solid particle suspension), which is a water-based fluid containing a colloidal suspension of CuO (copper oxide) particles, comprising 1 % of the total entrapped volume (or 0.01 times the total volume). Here, CuO nanoparticles are utilized for improving the thermal performance of carrier fluid and offset the damping impact of Lorentz force. Notably, this study models the base fluid and the nanoparticle dispersion as a single-phase

Table 1
Properties (thermophysical) of water and CuO nanoparticles [30].

Properties	CuO	Water
c_p (J·kg^{-1}·K^{-1})	531.8	4179
μ (kg·m^{-1}·s^{-1})	–	8.55×10^{-4}
β (K^{-1})	1.8×10^{-5}	21×10^{-5}
k (W·m^{-1}·K^{-1})	76.5	0.613
σ (μ·Scm^{-1})	2.7×10^{-8}	0.05
ρ (kg·m^{-3})	6320	997.1

Table 2
Correlations for the effective thermodynamic properties of CuO–water nanofluid [30].

Effective thermodynamic properties	Correlations for CuO–water nanofluid
Density (ρ)	$\rho = (1-\varphi)\rho_f + \varphi\rho_s$
Specific heat capacity (ρc_p)	$(\rho c_p) = (1-\varphi)(\rho c_p)_f + \varphi(\rho c_p)_s$
Thermal expansion coefficient (ρβ)	$(\rho\beta) = (1-\varphi)(\rho\beta)_f + \varphi(\rho\beta)_s$
Thermal conductivity (k)	$k = k_f\left[\frac{(k_s+2k_f)-2\varphi(k_f-k_s)}{(k_s+2k_f)+\varphi(k_f-k_s)}\right]$
Electrical conductivity (σ)	$\sigma = \sigma_f\left[1+\frac{3(\sigma_s/\sigma_f-1)\varphi}{(\sigma_s/\sigma_f+2)-(\sigma_s/\sigma_f-1)\varphi}\right]$
Thermal diffusivity (α)	$\alpha = \frac{k}{(\rho c_p)}$
Viscosity (μ)	$\mu = \frac{\mu_f}{(1-\varphi)^{2.5}}$

flow [30]. Furthermore, radiation and viscous dissipation effects have very little of an impact, and the effects of the Hall effect and Joule heating are also minimal [31]. The fundamental governing equations are derived from principles of fluid mechanics (fluid flow) and thermodynamics (heat transfer) that describe the overall thermo-fluid flow phenomenon [32]. The governing equations in dimensional forms are expressed [33–35] as

$$\frac{\partial u}{\partial x}+\frac{\partial v}{\partial y}=0 \tag{1}$$

$$\rho\left(u\frac{\partial u}{\partial x}+v\frac{\partial u}{\partial y}\right)=-\frac{\partial p}{\partial x}+\mu\left(\frac{\partial^2 u}{\partial x^2}+\frac{\partial^2 u}{\partial y^2}\right)+\sigma B^2\left(v\sin\lambda\cos\lambda-u\sin^2\lambda\right) \tag{2}$$

$$\rho\left(u\frac{\partial v}{\partial x}+v\frac{\partial v}{\partial y}\right)=-\frac{\partial p}{\partial y}+\mu\left(\frac{\partial^2 v}{\partial x^2}+\frac{\partial^2 v}{\partial y^2}\right)+\sigma B^2\left(u\sin\lambda\cos\lambda-v\cos^2\lambda\right)+g\rho\beta(T-T_c) \tag{3}$$

$$u\frac{\partial T}{\partial x}+v\frac{\partial T}{\partial y}=\alpha\left(\frac{\partial^2 T}{\partial x^2}+\frac{\partial^2 T}{\partial y^2}\right) \tag{4}$$

To non-dimensionalize these equations, the following dimensionless variables are introduced for coordinates (X, Y), velocity (U, V), pressure (P), and temperature (θ):

$$(X,Y)=(x,y)/H;\ (U,V)=(u,v)/U_0$$
$$\theta=(T-T_c)\Big/(T_h-T_c);\ P=(p-p_a)H^2\Big/\rho\alpha_f^2 \tag{5}$$

Consequently, the non-dimensionalized form of the equations [25, 26] is expressed as:

$$\frac{\partial U}{\partial X}+\frac{\partial V}{\partial Y}=0 \tag{6}$$

$$\left(U\frac{\partial U}{\partial X}+V\frac{\partial U}{\partial Y}\right)=-\frac{\partial P}{\partial X}+\frac{\nu_r}{\mathrm{Re}}\left(\frac{\partial^2 U}{\partial X^2}+\frac{\partial^2 U}{\partial Y^2}\right)-\frac{\sigma_r}{\rho_r}\frac{\mathrm{Ha}^2}{\mathrm{Re}}\left(V\sin\lambda\cos\lambda-U\sin^2\lambda\right) \tag{7}$$

$$\left(U\frac{\partial V}{\partial X}+V\frac{\partial V}{\partial Y}\right)=-\frac{\partial P}{\partial Y}+\frac{\nu_r}{\mathrm{Re}}\left(\frac{\partial^2 V}{\partial X^2}+\frac{\partial^2 V}{\partial Y^2}\right)-\frac{\sigma_r}{\rho_r}\frac{\mathrm{Ha}^2}{\mathrm{Re}}\left(U\sin\lambda\cos\lambda-V\cos^2\lambda\right)+\frac{(\rho\beta)}{\rho\beta_f}\frac{\mathrm{Ra}}{\mathrm{PrRe}^2}\theta \tag{8}$$

$$\left(U\frac{\partial\theta}{\partial X}+V\frac{\partial\theta}{\partial Y}\right)=\frac{\alpha_r}{\mathrm{RePr}}\left(\frac{\partial^2\theta}{\partial X^2}+\frac{\partial^2\theta}{\partial Y^2}\right) \tag{9}$$

Here, Pr is the Prandtl number, Re is the Reynolds number, Ra is the Rayleigh number, and Ha is the Hartmann number. These numbers are defined as:

$$\mathrm{Pr}=\frac{\nu_f}{\alpha_f};\ \mathrm{Re}=\frac{U_0H}{\nu_f};\ \mathrm{Ra}=\beta_fH^3(T_h-T_c)\frac{g}{\nu_f\alpha_f};\ \mathrm{Ha}=BH\sqrt{\sigma_f\Big/\mu_f} \tag{10}$$

The host fluid (water) and CuO nanoparticles make up the working medium (CuO-water nanofluid); the concentration φ indicates the volume-based presence of the nanoparticles. The thermophysical properties of the fluid phase and two types of nanoparticles (CuO) are shown in Table 1 [30]. Table 2 represents the typical correlations from the open literature, which is used to assess the effective qualities of the nanoliquid.

Table 3
Comparison of maximum stream function ψ_{max} with Ghasemi et al. [42] for different Ha and φ at $\mathrm{Ra}=10^5$.

Ha	Ghasemi et al. [42]		Present simulation	
	$\varphi=0$	$\varphi=0.02$	$\varphi=0$	$\varphi=0.02$
0	11.053	11.313	11.014	11.275
30	5.710	5.682	5.693	5.878
60	2.518	2.518	2.614	2.677

Table 4
Comparison of Nu with the data from Torki and Etesami [43].

Ra $\times10^7$	Nu for Pure Water ($\varphi=0$)			Ra $\times10^7$	Nu for Nanofluid ($\varphi=0.01$ %)		
	Present results	Torki and Etesami [43]	% Error		Present results	Torki and Etesami [43]	% Error
0.95	14.994	16.503	0.06	0.93	14.895	16.784	−2.68
1.77	17.769	18.814	5.88	1.98	18.312	20.577	−2.37
7.35	26.378	24.455	7.29	7.19	26.218	25.485	2.80

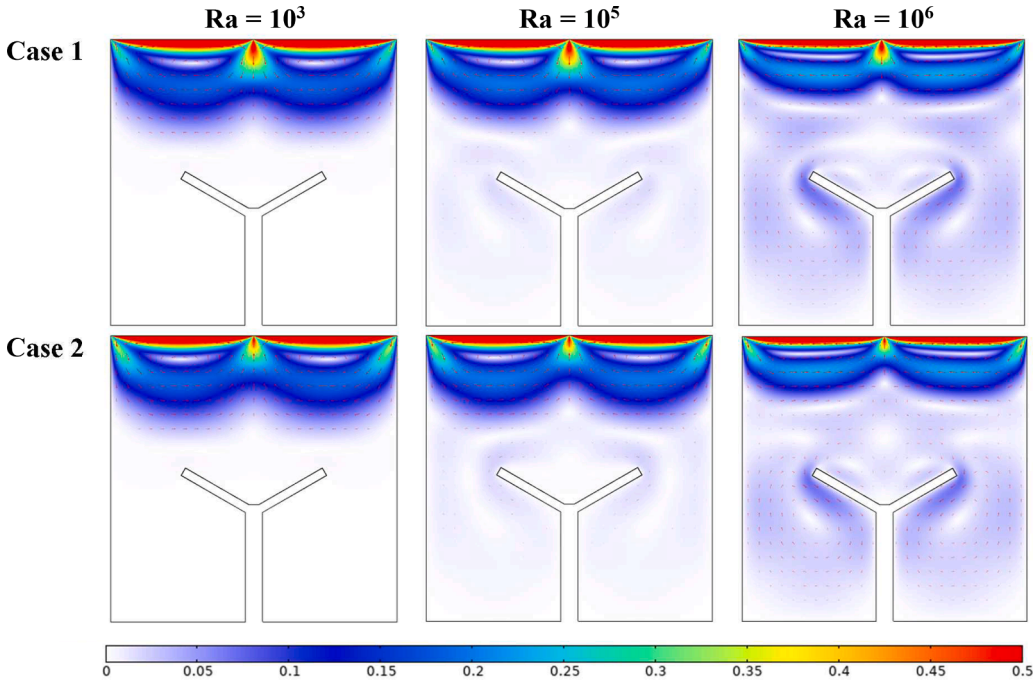

Fig. 2. Flow signature visualized through normalized velocity magnitude for the varying cases and Ra when Ha = 30, λ = 0°, Re = 50.

In this study, the system's irreversibility production (NS_{gen}) is also determined to assess the system's deviation from the reversible operation (ideal). This assessment is conducted considering the effects of fluid flow, and temperature gradients as magnetic fields [30]. Therefore, irreversibility production is evaluated in three forms: fluid friction (irreversibility due to viscous dissipation) (NS_v), irreversibility due to temperature gradient (NS_{tg}), and irreversibility due to magnetic field-induced (NS_m). The contributions of the local irreversibility generation rate (NS_{gen}) in non-dimensional (NS) forms are derived as [30]:

$$NS_{gen} = S \Big/ (k_f/H^2) = \overbrace{\frac{1}{(\theta+\theta_r)^2}\frac{k}{k_f}\left[\left(\frac{\partial\theta}{\partial X}\right)^2+\left(\frac{\partial\theta}{\partial Y}\right)^2\right]}^{NS_{th}} + \overbrace{\frac{\mathrm{EcPr}}{(\theta+\theta_r)}\frac{\mu}{\mu_f}\left[2\left(\frac{\partial U}{\partial X}\right)^2+2\left(\frac{\partial V}{\partial Y}\right)^2+\left(\frac{\partial U}{\partial Y}+\frac{\partial V}{\partial X}\right)^2\right]}^{NS_v} + \overbrace{\frac{\mathrm{EcPrHa}}{(\theta+\theta_r)}\frac{\sigma}{\sigma_f}(U\sin\lambda - V\cos\lambda)^2}^{NS_m} \tag{11}$$

The Eckert number (Ec) and temperature ratio reference parameter (θ_r) in Eq. (11) are defined as

$$\mathrm{Ec} = \alpha_f^2 \Big/ H^2 C_{Pf}(T_h - T_c) = \sqrt[3]{(g\alpha_f\beta_f)^2/(T_h - T_c)}\,\mathrm{Pr}^{-2/3}\mathrm{Ra}^{-2/3}$$
$$\theta_r = T_c/(T_h - T_c) \tag{12}$$

The total entropy generation (NS_{tot}) of the system is calculated as

$$NS_{tot} = \int\int NS_{gen}\,dX\,dY \tag{13}$$

Utilizing the average and local Nusselt numbers (Nu), which are given by, the local and average heat transfer over the active walls are calculated [36] as

$$\mathrm{Nu}_{loc} = \frac{k}{k_f}\left(-\frac{\partial\theta}{\partial n}\Big|_{\mathrm{hotwall}}\right) \tag{14}$$

$$\mathrm{Nu} = \frac{k}{k_f}\frac{1}{s}\int_0^S \left(-\frac{\partial\theta}{\partial n}\Big|_{\mathrm{hotwall}}\right) dS \tag{19}$$

where 'S' signifies active wall geometrical length. Streamlines are utilized to illustrate the local fluid flow patterns within the flow passage [37], and it is calculated using the stream function (ψ), which is expressed as

$$-\frac{\partial\psi}{\partial X} = V \text{ and } \frac{\partial\psi}{\partial Y} = U \tag{20}$$

ψ is taken as zero (0) at the walls to solve for the stream function. Furthermore, for the visualization of the structure of the heat energy transport process, Bejan's heat function (Π) [31,32] equations are solved and are expressed as

$$-\frac{\partial\Pi}{\partial X} = V\theta - \frac{\alpha_r}{\mathrm{RePr}}\frac{\partial\theta}{\partial Y} \text{ and } \frac{\partial\Pi}{\partial Y} = U\theta - \frac{\alpha_r}{\mathrm{RePr}}\frac{\partial\theta}{\partial X} \tag{21}$$

Finally, these heat functions are utilized to express the energy flux vectors [32].

3. Computational aspects and validation

The dimensionless governing Eqs. (6) through (9) are numerically resolved utilizing a finite element method (FEM)-based computational framework. With the specified boundary conditions in place, these transformed equations are addressed via the Galerkin weighted finite element method (FEM) [37,38]]. The governing equations are discretized across the domain of interest, which is meticulously divided into fine, non-uniformly distributed triangular meshes. The transformed equations are then solved at the nodal points of these triangular elements and along the bounding walls [39]. The numerical computations proceed through an iterative scheme employing the Newton–Raphson method, wherein the iteration process adheres to a convergence criterion that demands residual minimization to $\leq 10^{-6}$ [40,41].

To guarantee the precision of the simulation outcomes, an appropriately refined mesh is selected before undertaking the detailed analysis. This finely tuned mesh is optimized to capture the intricacies of

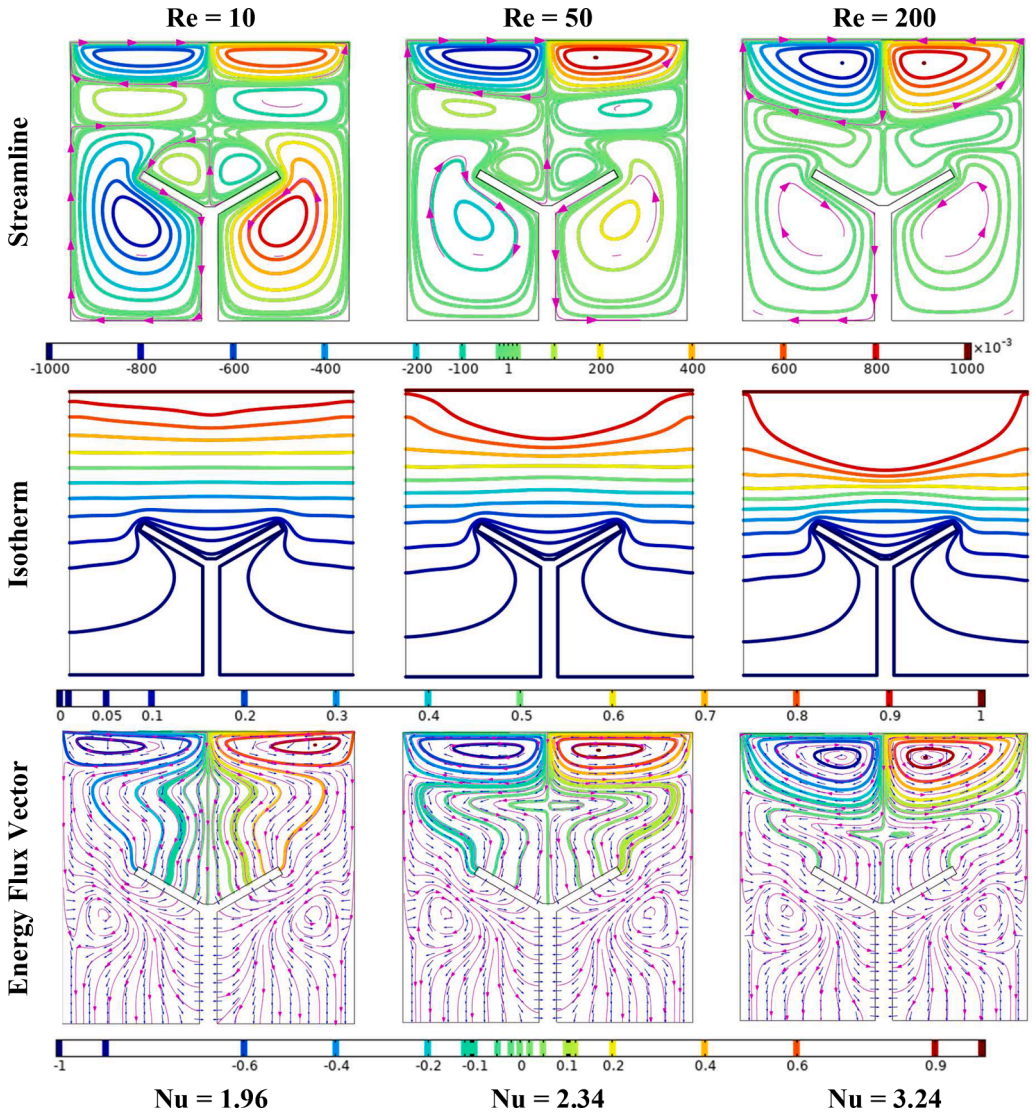

Fig. 3. Local contour plots of Case 1 for the varying Re when Ha = 30, λ = 0°, Ra = 10^6.

smaller-scale features, thereby obviating the necessity for an additional grid independence study. In this investigation, the mesh configuration encompasses a total of 6696 domain elements and 288 boundary elements. The minimum and maximum element sizes are determined to be 4×10^{-4} and 0.028, respectively.

In addition to conducting the grid independence study, the validation of the current model's solution methodology is meticulously undertaken. As an initial phase of this validation, the simulation of magnetohydrodynamic (MHD) buoyancy-driven convective phenomena within an enclosure containing an Al_2O_3/water nanofluid, as explored by Ghasemi et al. [42], is executed. The simulations encompass the computation of the average Nusselt number (Nu) at the heated boundary and the maximum stream function (ψ_{max}) across the flow domain under varying conditions of Hartmann number (Ha = 0, 30, and 60) and nanoparticle volume fraction (φ = 0 and 0.02) at a Rayleigh number of Ra = 10^5. The comparative analysis, as presented in Table 3, reveals a strong correlation between the current computational findings and the Nu and ψ_{max} values reported by Ghasemi et al. [42], thereby affirming the accuracy and reliability of the present computational model in predicting MHD thermal convection phenomena.

Moreover, the present numerical methodology has been juxtaposed with the experimental findings documented by Torki and Etesami [40], as delineated in Table 4. This comparative assessment pertains to a square enclosure containing both pure water (φ = 0) and SiO_2/water nanofluid (φ = 0.01 %). The maximum discrepancy observed between the current results and the experimental data is 7.29 % for pure water and 2.80 % for the nanofluid, respectively. It is crucial to acknowledge that the relatively higher maximum deviation is plausibly attributable to the inherent experimental uncertainties embedded within the data. This comparative analysis substantiates the precision of the current numerical approach in predicting heat transfer within a buoyancy-driven flow in an enclosure.

4. Results and discussion

The basic principle behind the present analysis is based on mixed convection, combined with magnetohydrodynamics. This approach explores the complex interplay between shear-driven flow, natural convection driven by buoyancy forces, and the effects of Lorentz forces due to the motion of an electrically conductive medium—specifically, the use of a smart fluid like nanofluid—under a magnetic field. A key feature of the study is the strategic placement of a Y-shaped obstacle along the bottom boundary of a square enclosure, which significantly influences the geometric configuration. An innovative aspect of the study is the inclusion of a top wall that is heated and split, capable of moving either to the right or left. In this context, U_l (= $-U_0$) represents the velocity of

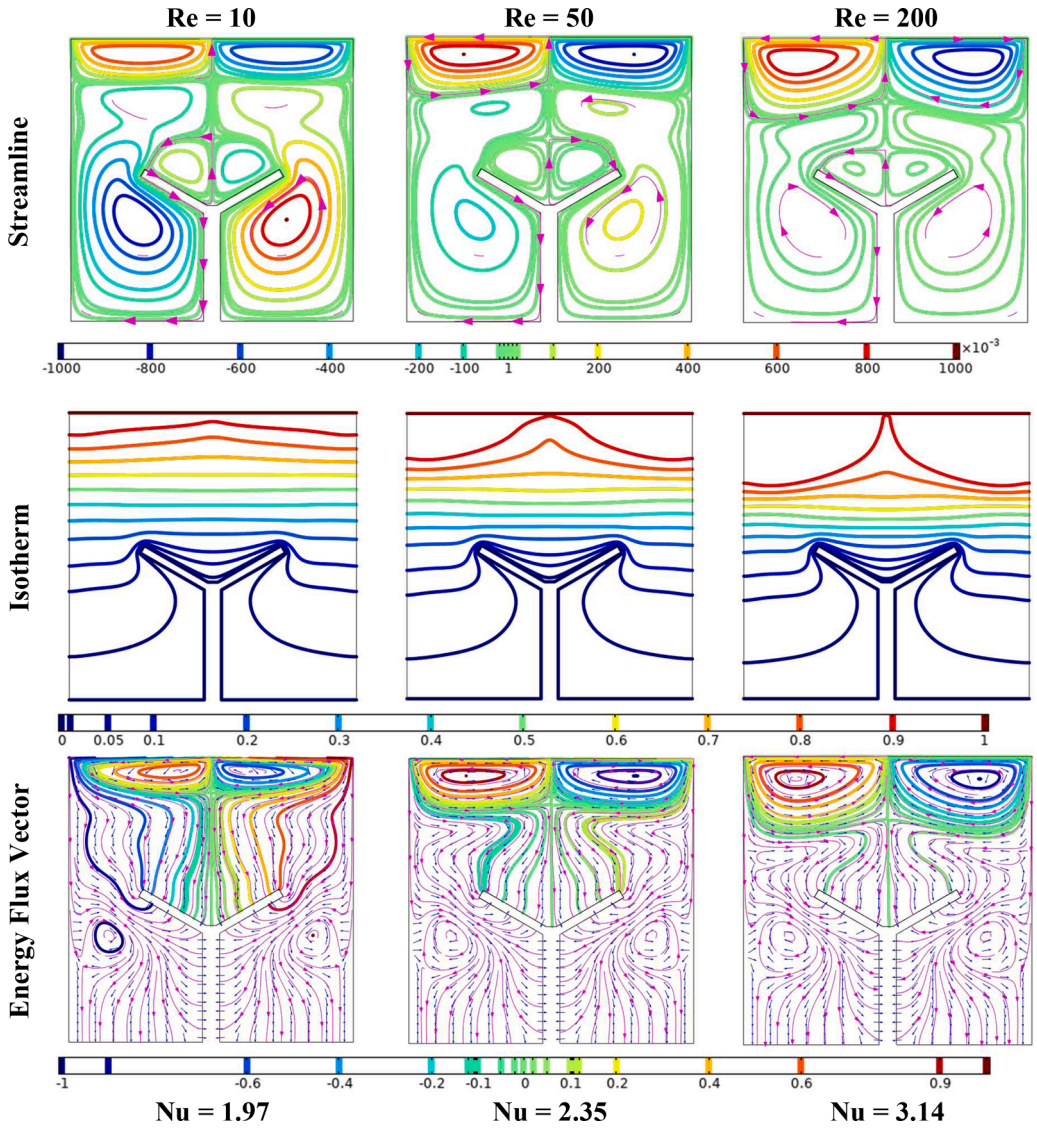

Fig. 4. Local contour plots of Case 2 for the varying Re when Ha = 30, λ = 0°, Ra = 10^6.

the left split wall, U_r (= $+U_0$) is the velocity of the right split wall, with positive values indicating rightward movement and negative values indicating leftward movement.

The classical benchmark problem of a single lid-driven cavity serves as an example of generating vortex or circulatory flow within a fluid-filled cavity. Initially, vortex formation occurs near the moving lid and gradually extends throughout the domain—a phenomenon extensively studied through both experimental and computational methods. Additionally, buoyancy forces, responsible for natural convection, induce movement in the fluid particles, typically leading to a circulatory pattern between the heated and cooled regions. The resulting flow pattern is influenced by the damping effects from the interaction between the nanofluid and the magnetic field, as well as the combined velocity components.

By applying non-dimensional analysis, we focus on three critical parameters that dictate the system's behavior: the Reynolds number (ranging from Re = 10 to 200), the Rayleigh number (ranging from Ra = 10^3 to 10^6), and the Hartmann number (ranging from Ha = 0 to 70), along with the magnetic field orientation (ranging from λ = 0 to 150°). The study is conducted for two scenarios: Case 1 with $U_l = +1$ and $U_r = -1$, and Case 2 with $U_l = -1$ and $U_r = +1$.

4.1. Flow signature

To facilitate understanding of the hydrothermal behavior in the split-driven cavity, Fig. 2 presents the flow signature within the cavity under two different directions of wall motion for varying Ra when Ha = 30, $\lambda = 0°$, and Re = 50. Essentially, Fig. 2 shows the normalized velocity magnitude plots of fluid flow (in the range of 0–1). The normalization is carried out using the maximum values, and thus all contour levels fall between 0 and 1, regardless of the maximum velocity. However, the scale is set from 0 to 0.5 for clarity in the velocity plot.

In general, the velocity vectors are used to determine the main impact of fluid flow direction caused by the direction of the wall motion. The vector arrowheads reflect the directions of fluid flow, which is modulated by the wall motion direction as well as the Ra value. For Case 1, the fluid flows from both left and right, and these flows collide about the middle point and go downward direction. On the other hand, at both upper corners, there is a suction effect due to the wall shearing force, and thus fluid rushes toward the corners. Such a change in flow directions causes the formation of two fluid circulations in the upper portion of the cavity. With the increasing Ra values, the strength of the fluid circulation and the flow velocity increase.

For Case 2, where the hot split walls are moving in opposite directions, a suction effect is created about the midpoint of the upper

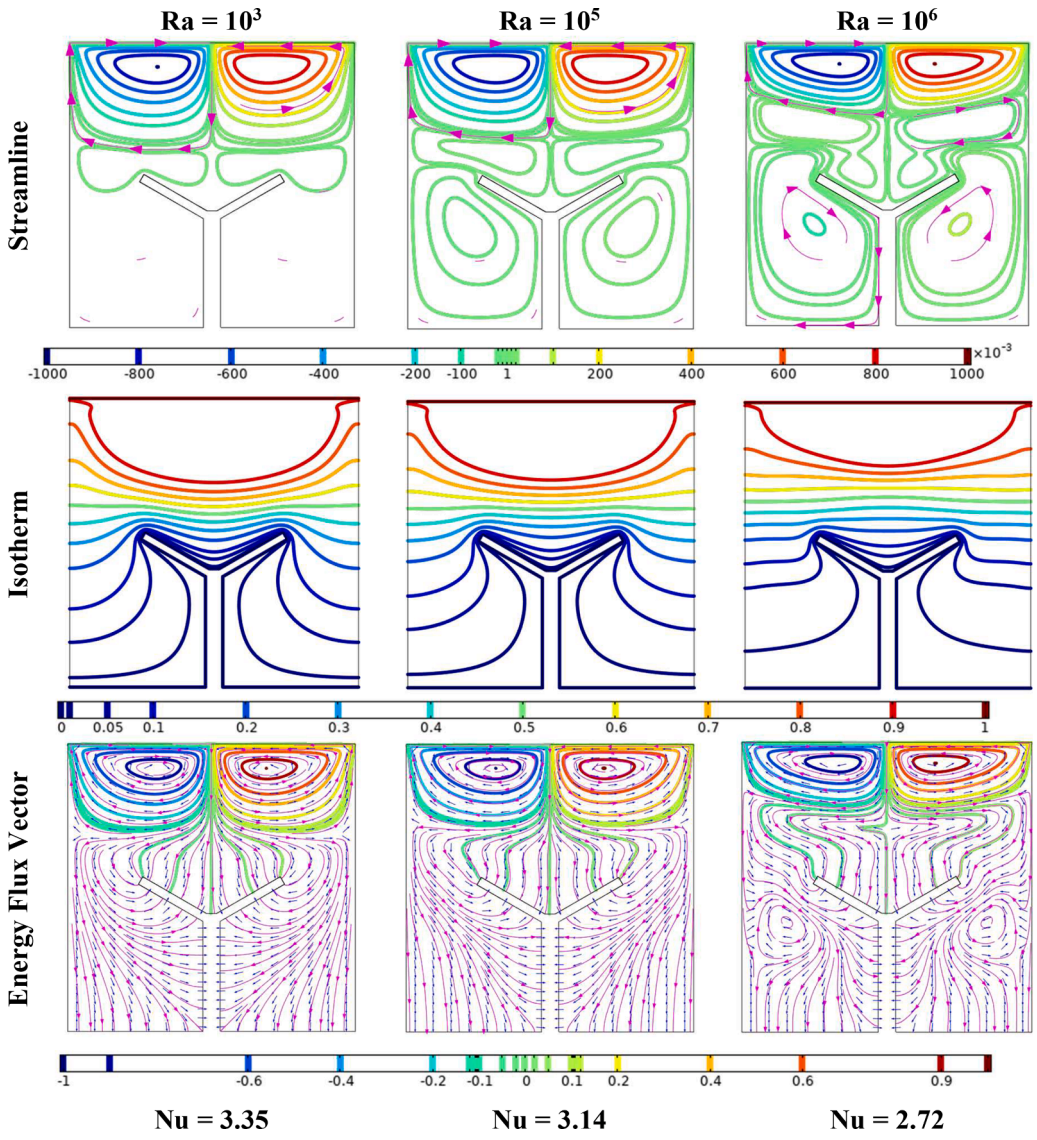

Fig. 5. Local contour plots of Case 1 for the varying Ra when Ha = 30, $\lambda = 0°$, Re = 100.

walls, and fluid is pulled towards the two ends of the walls. Thus, circulating cells form, but they are rotating in opposite directions. At higher Ra, weaker fluid circulations are also noted in the lower portion of the cavity.

4.2. *Influence of Reynolds number*

A detailed visualization of flow dynamics can be effectively achieved by analyzing streamlines, while a combined observation of isotherms, heat lines, and energy flux vectors provides deeper insights into the complexities of energy flow within the scenario. By varying the Reynolds number (Re = 10, 50, 200) while keeping Ha = 30, Ra = 10^6, and a magnetic field oriented at $\lambda = 0°$, distinct flow patterns are revealed. Under these specified conditions, the resulting flow patterns display notable symmetry. Case 1 and Case 2 represent the outcome in Fig. 3 and Fig. 4, respectively.

In Case 1, as the lid moves, clockwise vortices originate from the left lid, while the counterclockwise vortices form near the right lid. This pattern is reversed in Case 2. The flow domain is divided into regions of secondary circulations, where the fluid mass adjacent to each circulatory region supports the reversal of circulation in neighboring areas of the domain.

From an intuitive perspective, analyzing the flow pattern and the fluid release position by the split lid (at the mid-plane in Case 1 and at the walls in Case 2) reveals that an additional vortex layer forms in Case 1, while this layer is absent in Case 2 due to the smoother flow. The intensity of circulation increases with the rise in inertial forces, indicated by a higher Re, as demonstrated by the stream function (ψ) values. The magnitude supports this observation, showing that as Re increases from 10 to 100, while keeping other parameters constant, the circulation strength becomes more pronounced, as reflected in the corresponding ψ values.

Focusing on heat transfer, the isotherm contour analysis for Re = 10 shows a stratified zone between the top wall and the Y-shaped obstacle, with the isotherm distribution in the lower region shaped by the cold surface of the obstacle. As Re increases and the primary vortex near the lid strengthens, the heated fluid is pushed downward, compressing the isotherms and thereby enhancing the proportion of heated fluid, which in turn boosts the rate of heat transfer. This occurs because the energy exchange happens within a thinner fluid layer, leading to quicker temperature changes. The elevated Nusselt Number values, which indicate the rate of heat transfer, confirm this trend. A higher Re value suggests greater fluid mixing within the cavity, and the isotherm distribution in the upper part of the cavity is significantly affected.

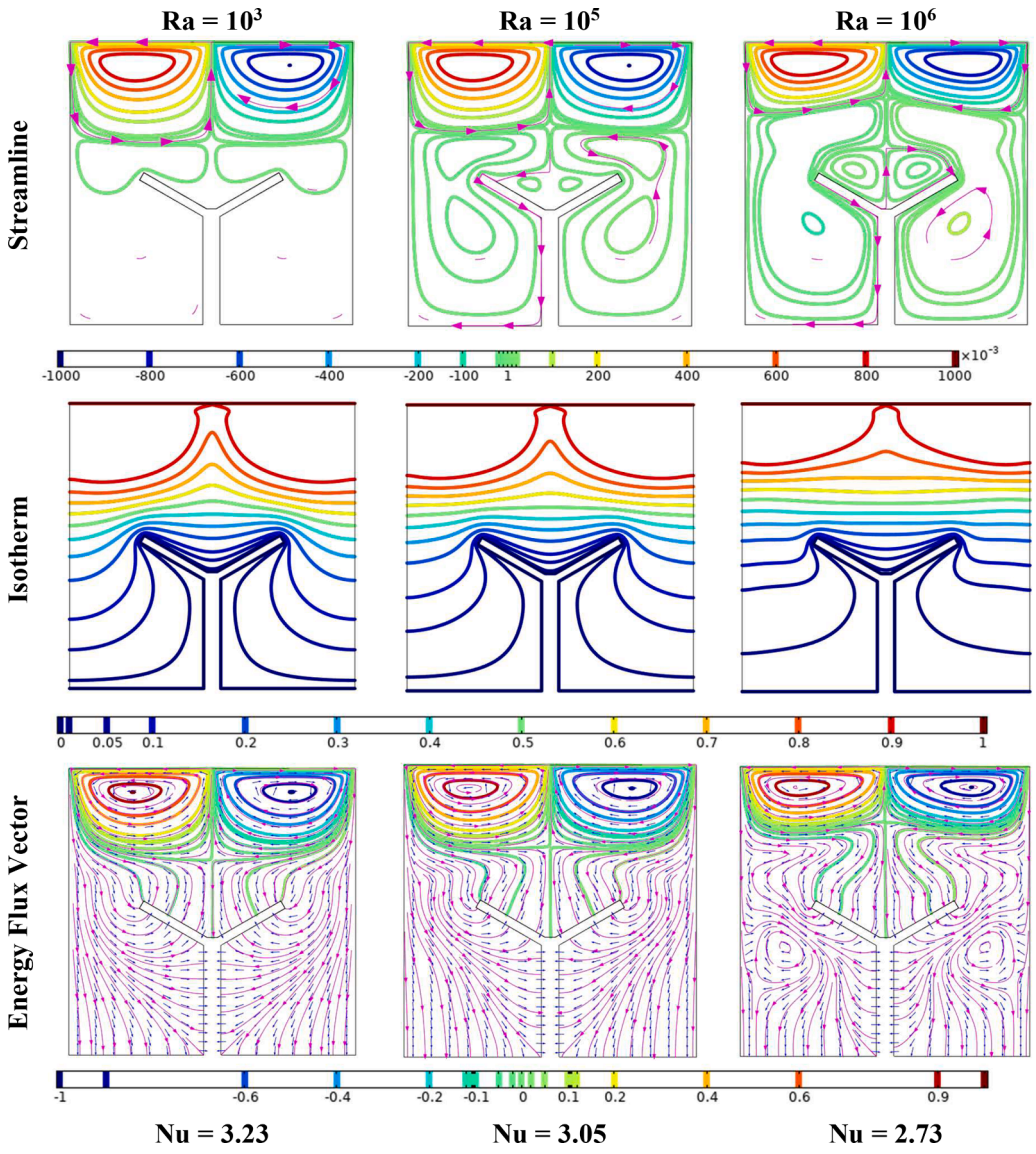

Fig. 6. Local contour plots of Case 2 for the varying Ra when Ha = 30, λ = 0°, Re = 100.

The energy flux vectors, along with the heat lines, illustrate the energy transfer path from the hot to the cold wall. After examining the flow characteristics within the domain, it is clear that the heat lines or energy flux vectors form a vortex structure near the lid, which explains the convective flow mixing and the associated energy transfer. The remaining heat lines represent the spontaneous transfer of heat from a higher to a lower temperature surface, primarily through conduction within the fluid.

As convection becomes more dominant with an increase in inertial forces, signified by a higher Re, the vortex domain for the heat lines expands. Similar variations are observed when transitioning from Case 1 to Case 2. For Re = 10, the initially stratified isotherms become highly curved, and the gap between isotherms widens, especially near the boundaries, where the fluid is released by the lid after being drawn from the mid-plane, as illustrated. The direction of energy flux also shifts due to the altered flow pattern, although the fundamental principles remain consistent. The increased flow mixing and the shift towards convective heat transfer over conduction result in a higher Nu.

4.3. Influence of Rayleigh number

The comprehensive discussion on flow dynamics, the identification of underlying mechanisms, and the observed variations with respect to Re has been thoroughly satisfying. What further enhances the present study is the intricate relationship between natural (or free) convection and forced convection. In this context, the temperature difference drives buoyancy forces within the flow domain, impacting the bulk of the nanofluid.

The Rayleigh number (Ra), a crucial parameter in this analysis, is the product of the Grashof number (Gr) and the Prandtl number (Pr). The Grashof number measures the relative strength of buoyancy forces compared to viscous forces in a fluid, while the Pr value indicates the ratio of momentum diffusivity (kinematic viscosity) to thermal diffusivity, thereby connecting fluid dynamics and heat transfer. As a result, the Ra value illustrates how a temperature gradient induces buoyancy forces within the fluid.

In Figs. 5 and 6, Cases 1 and 2 respectively depict the outcomes when the fluid in the cavity is subjected to Re = 100 and Ha = 30, with observations recorded for Ra = 10^3, 10^5, and 10^6. According to existing literature, at Ra = 10^3, the flow velocity is minimal, suggesting that buoyancy forces are weak, making conduction the dominant mode of heat transfer, as the fluid remains mostly static within the cavity under purely natural convection. However, in our model, the motion of the split lid introduces an additional physical effect, causing circulation in

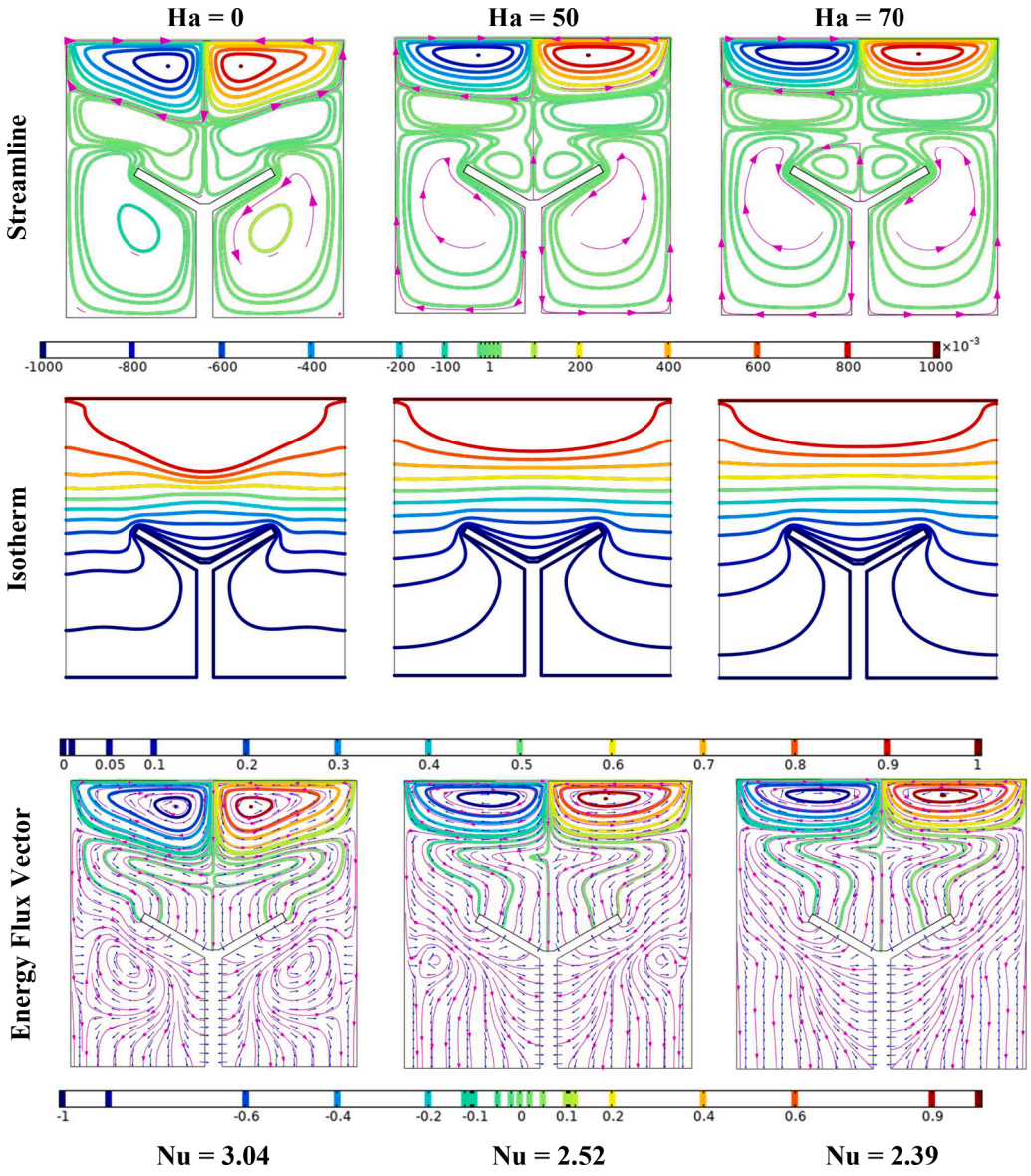

Fig. 7. Local contour plots of Case 1 for the varying Ha when Ra $= 10^6$, $\lambda = 0°$, Re $= 100$.

the upper region of the cavity and leading to vigorous flow mixing, although much of the fluid near the bottom wall experiences minimal velocity.

Buoyancy forces become significantly more influential when Ra exceeds 10^4, creating an intriguing flow pattern for Ra $= 10^5$, and 10^6, where a larger portion of the fluid actively engages in the overall phenomenon. Interestingly, in all three scenarios, the vortex regions experience a slight reduction in thickness, likely due to the increased upward momentum of the fluid.

At Ra $= 10^3$, the isotherms are closer together near the valley of the Y (the top V-shaped region), likely due to the dominance of inertial forces and the minimal impact of buoyancy. These inertial forces are generated by the downward movement of the fluid, driven by the lid. As buoyancy forces strengthen, the fluid motion and flow mixing near the cavity lid decrease. Since the directions of inertial and buoyancy forces are opposed, increasing the Rayleigh Number leads to more stratified isotherms, reducing the heat transfer rate as convective effects diminish.

Interestingly, in a cavity governed solely by natural convection, the heat transfer rate usually increases with a rising Ra, which contrasts with our current case. This difference results from the vector addition of forces within the domain, where the direction of each driving force plays a crucial role. This observation is further supported by the decrease in Nusselt Number values in our current scenario.

The analysis of energy flux vectors reveals similar patterns, with the thinning of vortices as the Rayleigh Number increases, driven by the same mechanism that affects the streamlines. The reduction in flow mixing due to buoyancy is evident from the distribution of heat lines, particularly in cases where Ra is 10^5 or higher. The confinement of vortices to a smaller region suggests that energy circulation is limited to that specific area, without being effectively carried forward by the fluid.

4.4. Influence of Hartmann number

Having thoroughly examined the impact of the Reynolds and Rayleigh numbers, we now turn our attention to an equally important aspect of magnetohydrodynamics: the influence of the magnetic field on the model. In physics, it is well-known that any charged particle moving within an electromagnetic field experiences a force known as the Lorentz force. This force is crucial in our model, where we use a nanofluid with electrical conductivity. For a substance to conduct electricity, it must have free electrons, which is typically seen in metals.

In this model, as the fluid, driven by mixed convection, moves

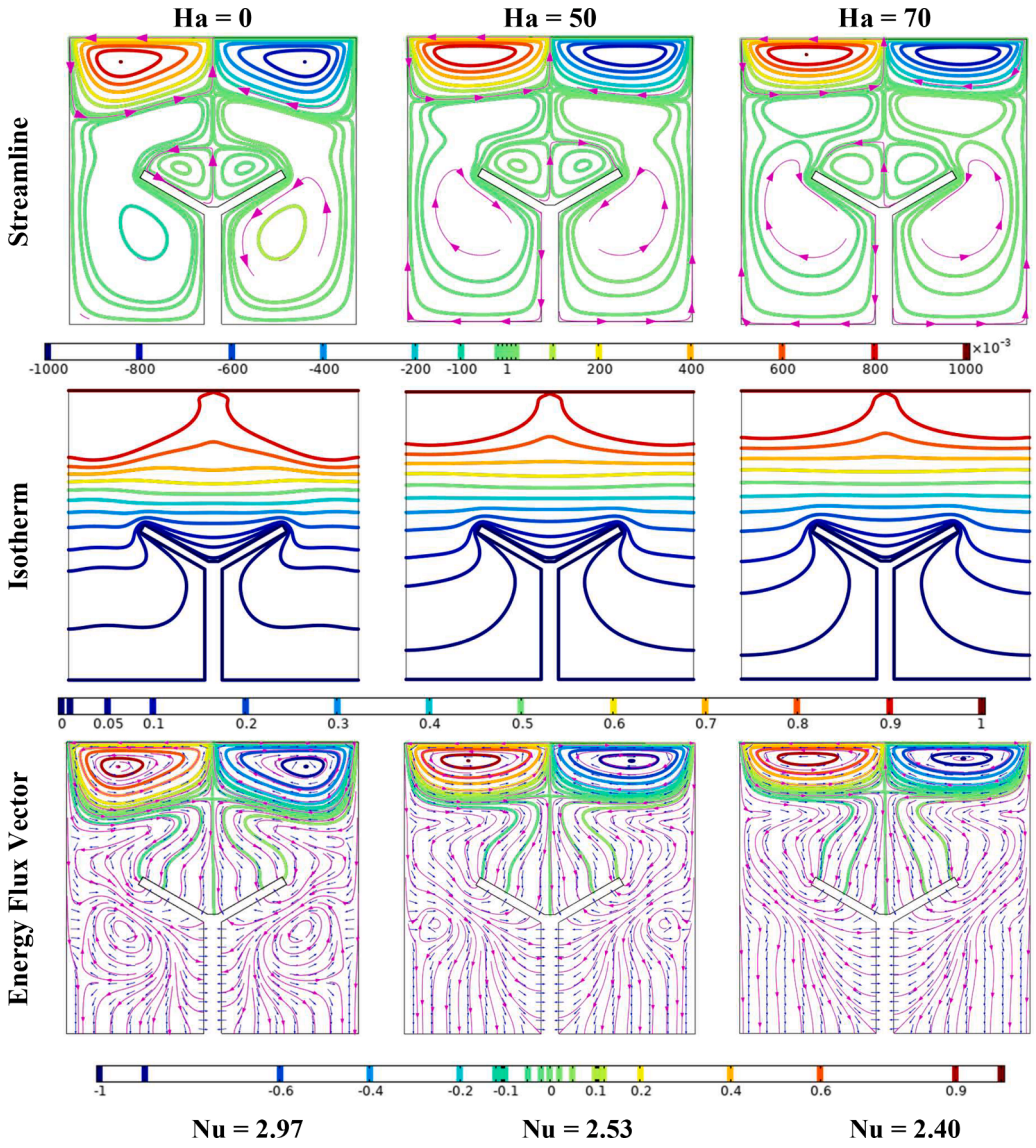

Fig. 8. Local contour plots of Case 2 for the varying Ha when Ra = 10^6, λ = 0°, Re = 100.

through the cavity, it encounters a force that acts perpendicular to its direction of motion. This interaction often leads to flow dampening, where the fluid's movement is slowed or resisted, resulting in reduced flow mixing quality compared to cases without a magnetic field. The results confirm this damping effect, as the stream function (ψ) values decrease with an increase in the Hartmann number (Ha).

Figs. 7 and 8 illustrate the effects for Ha values of 0, 50, and 70 while keeping the Ra = 10^6 and the Re = 100. As discussed earlier, it is evident that for Ra = 10^6, the Nusselt number (Nu) decreases compared to when Ra = 10^3. Additionally, the patterns of streamlines and heat lines for Ha > 0 show a reduction in the vortex domain, leading to much less mixing due to the damping force. The isotherm distribution also aligns with our previous analysis, becoming more flattened as Ha increases from 10 to 70, which in turn reduces the rate of heat transfer.

The streamlines indicate a significant weakening of flow strength, as seen in the recirculatory patterns formed. Thus, what was once vigorous flow is significantly dampened by the Lorentz force induced by the magnetic field. This effect is particularly pronounced as Ha increases from 50 to 70, where we observe a marked reduction in the intensity and extent of the flow patterns.

4.5. Influence of magnetic field inclination

After thoroughly examining the impact of the magnetic field strength on the flow domain and providing well-founded explanations, we can further modulate this effect by introducing an inclined magnetic field (as shown in Figs. 9 and 10). The magnetic field is oriented at various angles relative to the bottom wall of the cavity, specifically at λ = 30°, 90°, and 150°, while keeping the parameters constant at Ra = 10^6, Ha = 30, and Re = 100.

The observations reveal that as the inclination angle increases, particularly in the first quadrant, the circulation intensity progressively decreases. The streamline patterns show considerable distortion in response to the angle of inclination, with a noticeable weakening of the flow due to this orientation.

Similarly, the isotherm patterns exhibit slight distortions when compared to the 0° configuration. However, the Nusselt number increases with the angle, indicating improved flow mixing. This trend continues up to 90°, after which the values begin to decrease, following a nearly symmetrical pattern, as seen with similar effects at 30° and 150° (i.e., 180° - 30°). The heat lines and energy flux vectors also show these distortions.

Moreover, the rate of change in the Nusselt number slows after 75°,

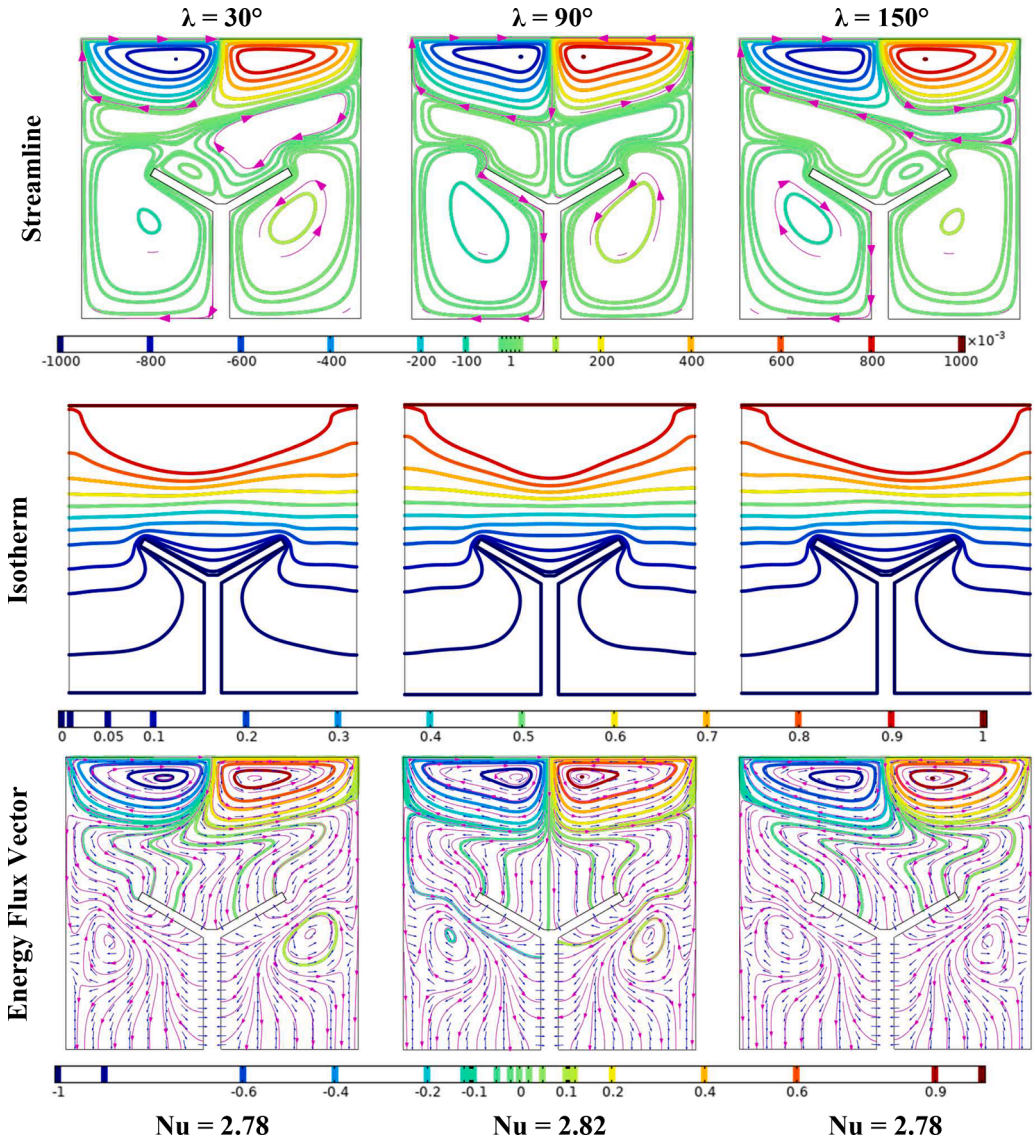

Fig. 9. Local contour plots of Case 1 for the varying λ when Ra = 10^6, Ha = 30, Re = 100.

eventually stabilizing, suggesting a reduced variation in its value beyond this point. This observation provides valuable insight into the optimal angle for magnetic field orientation to enhance heat transfer in such systems.

4.6. Overall heat transfer analysis

The Nusselt number (Nu), whether considered locally or as an average, is an invaluable metric in physical analysis. This dimensionless number provides a simplified alternative to more complex measurement models, allowing for a comprehensive examination of heat transfer characteristics across various flow domains under various parametric scenarios. Fig. 11 illustrates the variation of the average Nu values for varying Re across different Ra, Ha, and λ.

Starting with the impact of Re, significant variations are noted when other parameters remain constant. Specifically, the average Nu shows a substantial increase in Case 1 where Ra = 10^6, Ha = 30, and $\lambda = 0^\circ$ For example, as Re increases through the sequence (10, 50, 100, 200), a noticeable rise in Nu occurs. This increase can be attributed to the enhanced flow mixing caused by the significantly stronger inertial forces within the fluid.

When considering the case where Ra increases according to the sequence (10^3 to 10^6) while keeping Re = 100, Ha = 30, and $\lambda = 0^\circ$, a decrease in Nu is observed. This reduction is associated with diminished flow mixing, resulting from the opposing effects of inertial and buoyancy forces, the latter being influenced by Ra. Additionally, the energy transfer rates decline further as the magnetic field's strength increases.

The trend of increasing Nu with increasing Re is true for both Cases 1 and 2 (Figs. 11a and 11b). However, the peak value of Nu is noted for Case 1 (= 4.018) compared to Case 2 (3.534). Therefore, this finding establishes that Case 1 could be opted for enhancing heat transfer when Ra is lower.

As Ha grows, the Lorentz force dampens the flow, leading to a corresponding drop in Nu. The effect of Ha on Nu is shown in Figs. 11c and 11d when Ra = 10^5, and $\lambda = 0^\circ$ The trend of Nu drop is quite interesting. For Case 1, Nu drops sharply from 11.927 to 3.750 at Ha = 30 and Re = 200. After Ha = 30, the decrement in Nu is not so high. This trend is similar for Re = 100 and 50. In the case of Re = 10, the change in Nu is insignificant. This is due to the lesser effect of shear force on the fluid flow. Furthermore, after Ha = 30, the fluid flow strength is reduced significantly due to the strong Lorentz force. In Case 2, the magnitude of Nu drops from 7.037 to 3.402 at Ha = 30. In general, Case 1 offers higher heat transfer for lower Ha and higher Re values.

However, as the inclination angle of the magnetic field (λ) increases

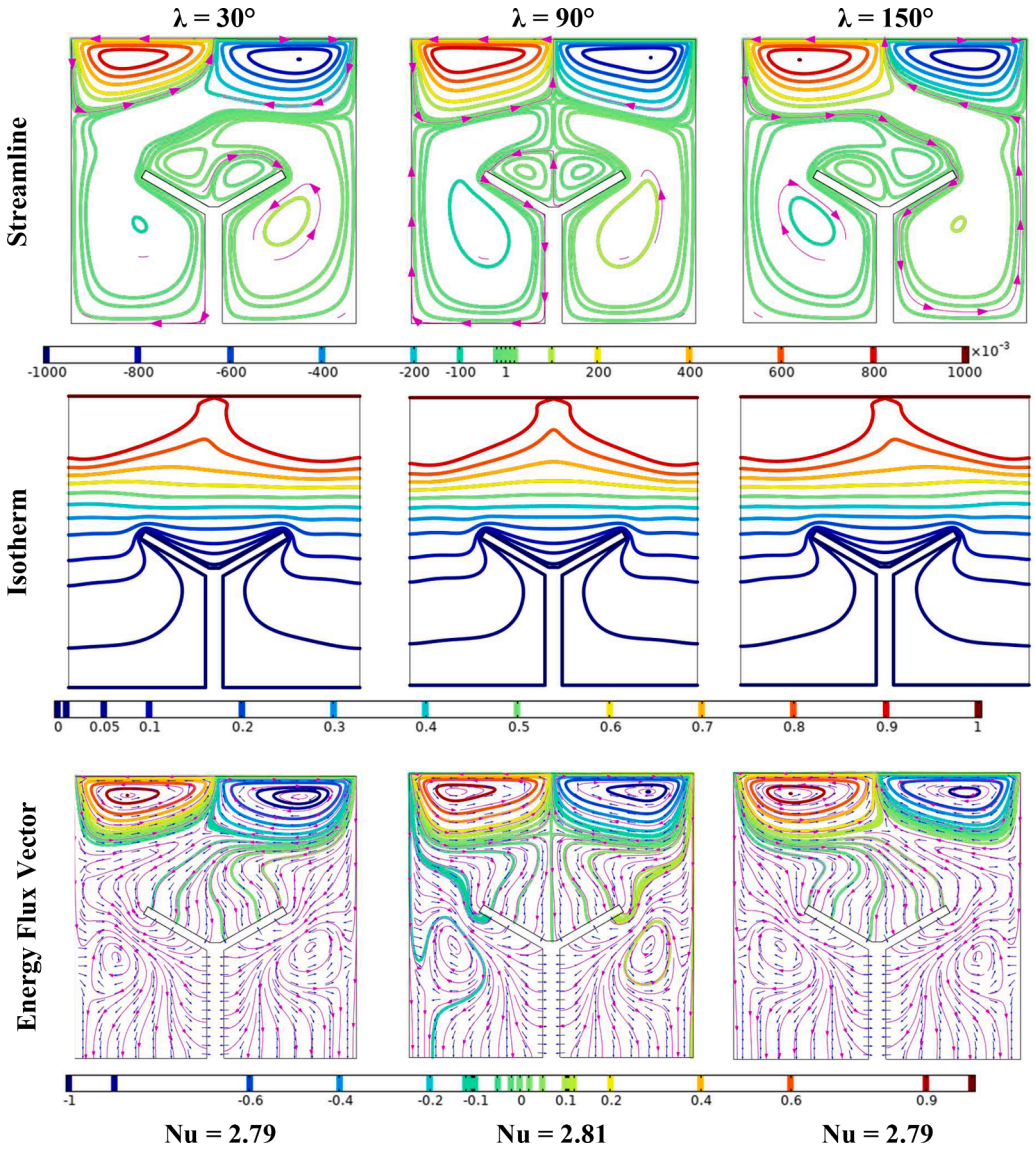

Fig. 10. Local contour plots of Case 2 for the varying λ when Ra = 10^6, Ha = 30, Re = 100.

(as shown in Figs. 11e and 11f), likely due to gravitational effects and reduced magnetic interference, the average Nu rises to about 75° Beyond this angle, it fluctuates slightly within that range until reaching 90°, after which the increase slows, and the value begins to decrease again. A similar trend is noted for Case 1 and Case 2. However, the highest Nu value is achieved for Re = 200 and $\lambda = 75°$ Due to the change in orientation of the magnetic field, the sharing of the Lorentz force changes from the y-direction to the x-direction and the fluid flow circulation becomes asymmetric type, which alters the heat transfer characteristics.

4.7. Entropy generation analysis

The principles of thermodynamics, which govern natural phenomena, emphasize that energy flow follows specific, natural laws that are inherently spontaneous. This characteristic is closely associated with entropy, a fundamental thermodynamic property that quantifies the degree of irreversibility in a system. To fully understand the processes involved, this study focuses on analyzing entropy generation within the system.

The visual data illustrate the contributions of viscous (Figs. 12 and 13), magnetic (Figs. 14 and 15), and total entropy (Figs. 16 and 17) generation under various scenarios. The entropy generation contour plots for viscous irreversibility indicate that depending on parameters such as Re, Ra, and Ha, the primary viscous irreversibility occurs near the moving boundary (split lid), where the rapid fluid motion driven by the lid is significant. Magnetic effects on entropy generation are most noticeable at the regions where the lid's motion begins or ends. The plots for different Ha values, with Re and Ra constant, reveal that as the magnetic field strength increases, entropy generation within the domain decreases, likely due to the magnetic field's damping effect.

Moreover, increases in Re and Ra lead to greater irreversibility in the upper flow domain, with some entropy generation occurring in the bulk flow, especially at lower Re and higher Ra. An important finding from the plots is that when the direction of the lid's motion changes (Cases 1 and 2), the entropy generation contours on the top surface also shift accordingly.

The total entropy generation analysis shows that for Ra = 10^4 and Re = 10, where conduction primarily drives the flow, thermal entropy governs the effects, distributed mostly in the upper region of the domain.

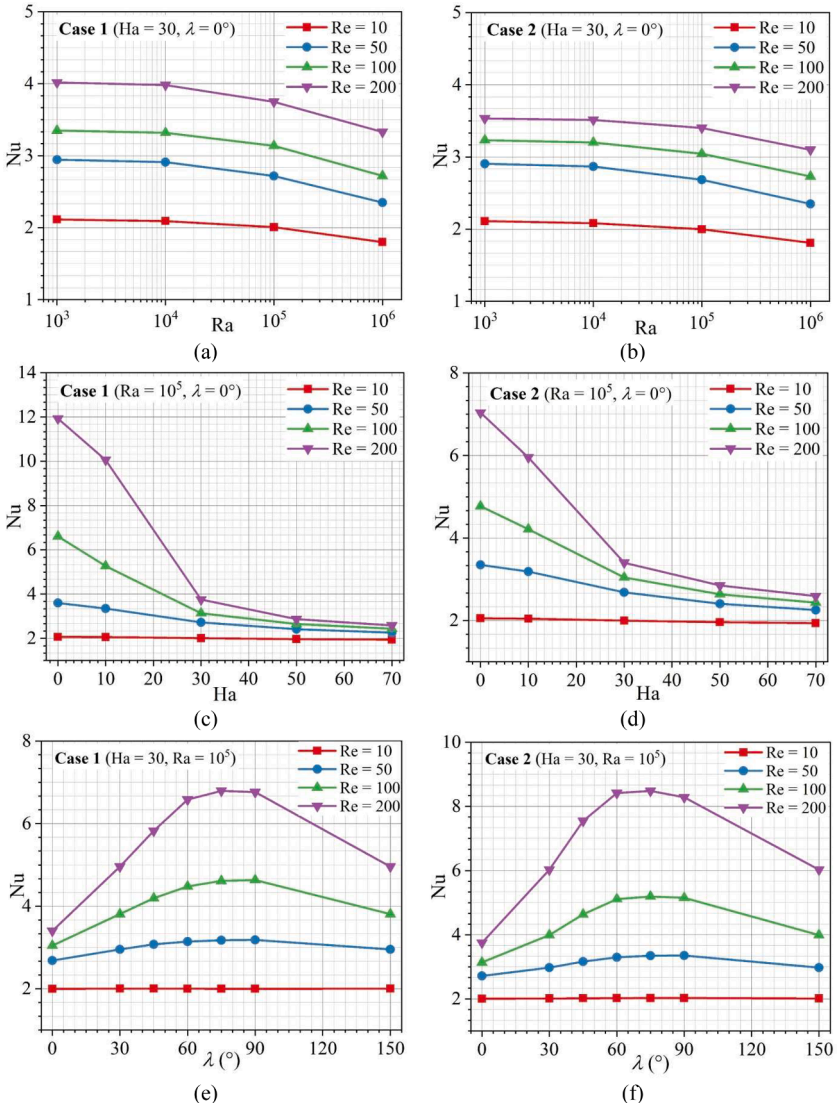

Fig. 11. Overall heat transfer characteristics represented by Nu for the varying Re and cases with different values of Ra (a, b), Ha (c, d), and λ (e, f).

High irreversibility is observed where the fluid is released by the lid and where it initially impacts the Y-shaped obstacle during mixing. However, this effect is gradually reduced with increasing Ha, as shown by the contour plots.

With higher inertial forces pushing the flow into the valley of the Y-shaped obstacle, entropy generation becomes concentrated at the wings of the Y. Conversely, increasing Ha significantly dampens this effect, resulting in a more even distribution of entropy generation in the upper region. The overall pattern remains consistent, with more intense effects seen at lower Ha, higher Re, and lower Ra. As Ra increases, enhancing buoyancy, the overall irreversibility decreases.

In summary, conditions that disrupt natural flow patterns or increase resistance lead to greater irreversibility. Complex geometries with sharp angles or corners exacerbate this effect due to flow separation, while intricate boundary conditions contribute to substantial entropy generation. A detailed examination of the causes and regions of entropy loss is essential for optimizing the model, which can then be applied to real-world situations. Simulation software data reveal trends related to the three non-dimensional parameters discussed. Specifically, altering the magnetic field direction up to 60° slightly increases entropy generation compared to other angles, with all other parameters held constant. The graphical data analysis offers deeper insights into the behavior of the system.

For understanding the impact of all the parametric variations on the overall thermal performance as well as irreversibility productions, Tables 5 and 6 depict the selected global summary of the results through Nu, $|\psi_{\max}|$, NS_v, NS_m, NS_{th}, and NS_{tot} for Case 1 and Case 2. Generally, increasing Re leads to a stronger impact of external force on the fluid circulation through the wall translation. Thus, higher Re leads to higher Nu values and the corresponding NS_{tot} is also higher. Increasing Ra harms the heat transfer, because of the reduction in fluid mixing. On the other hand, magnetic field intensity increase always dampens the heat transfer, which is compensated by the increasing inclination of the magnetic field, particularly when Ha = 30 and $\lambda = 75^\circ$ and Re = 200. The trend of the heat transfer as well as irreversibility production is similar for Case 2 also but with reduced magnitudes.

Therefore, this finding establishes that Case 1 could be opted for enhancing the heat transfer when Ra is lower, and Re is higher and it is further modulated by the magnitudes of Ha and its inclination.

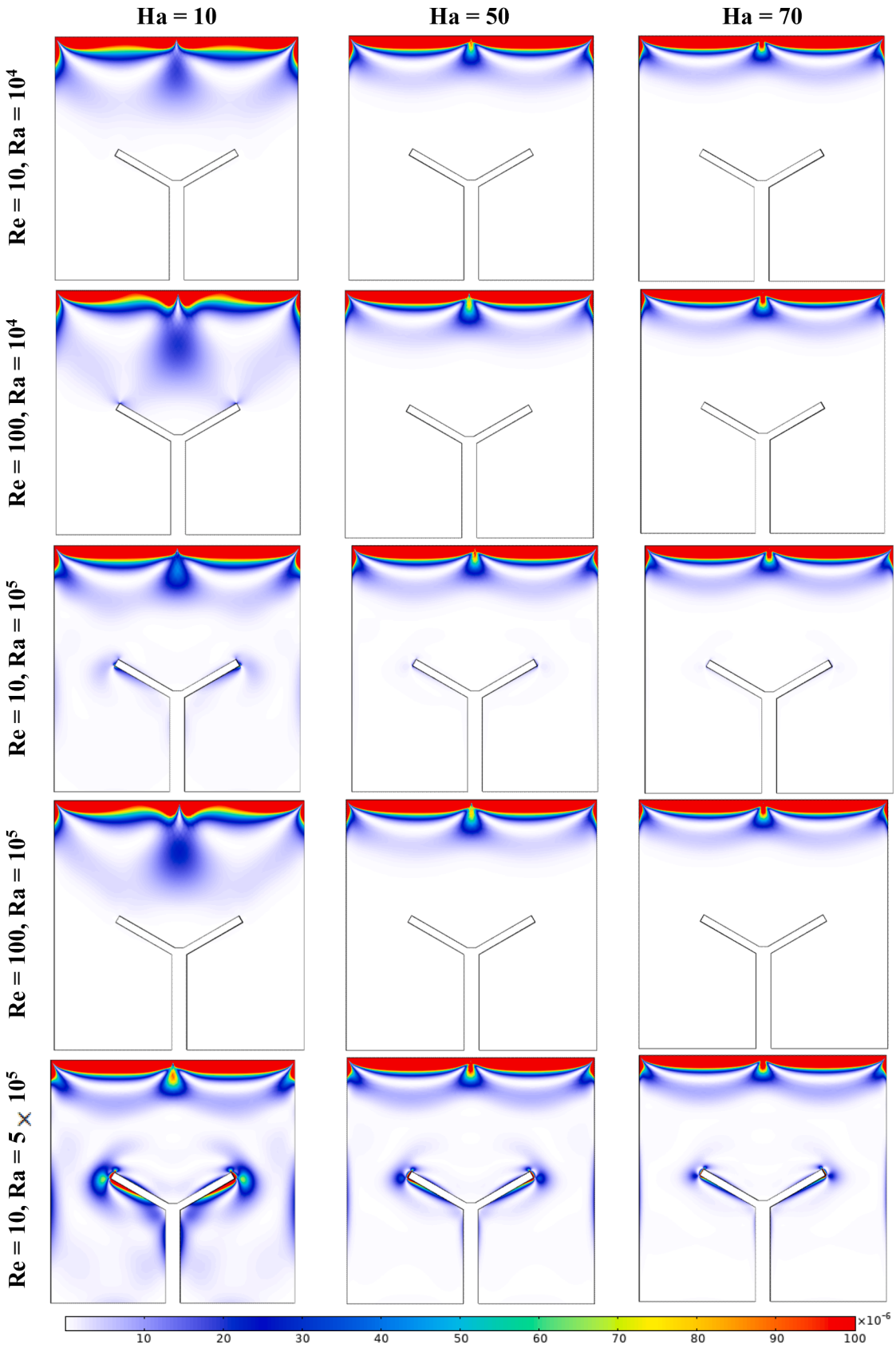

Fig. 12. Local contour plots for viscous irreversibility, taking deferent values of Ra, Ha, and Re for Case 1 when $\lambda = 0°$

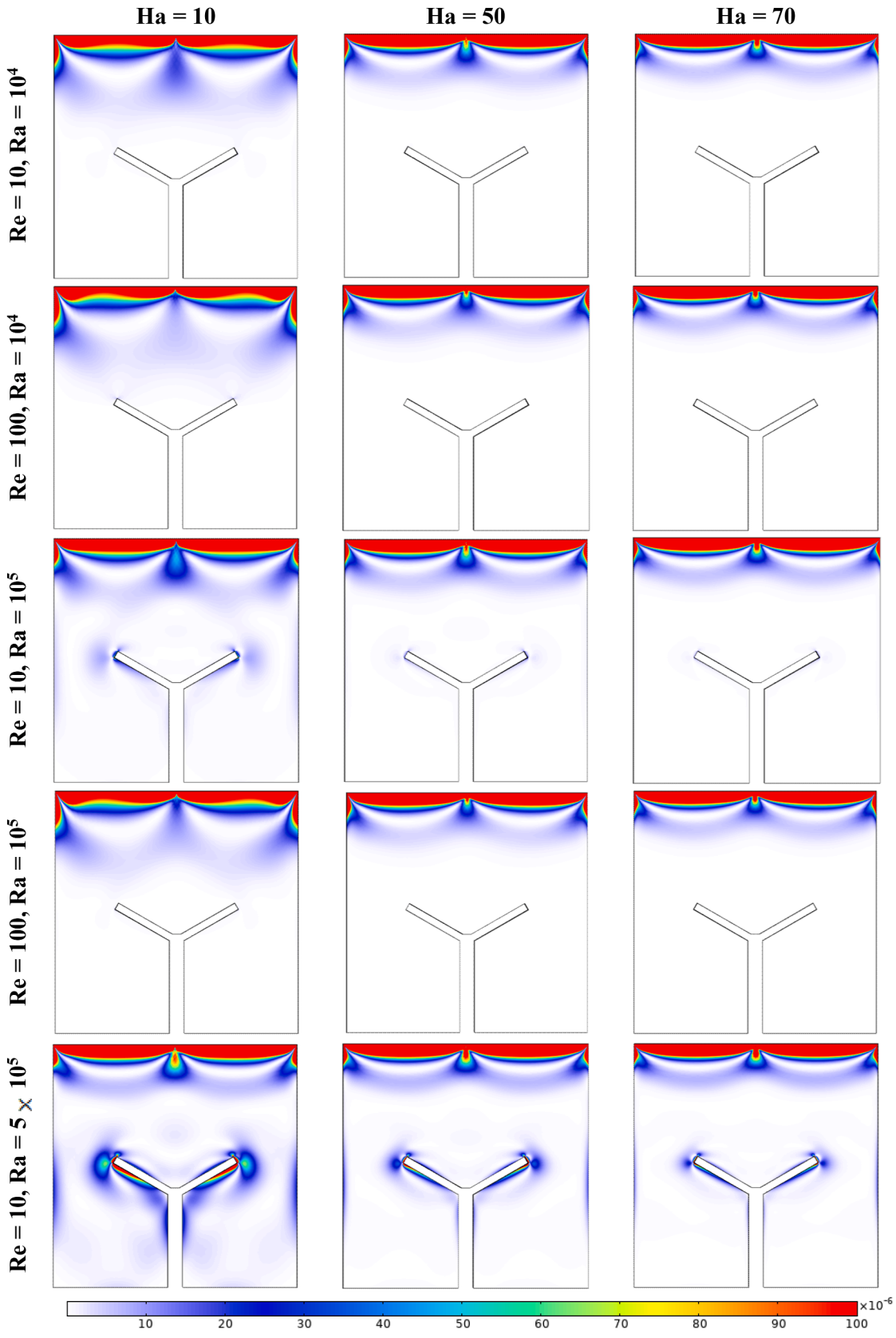

Fig. 13. Local contour plots for viscous irreversibility, taking deferent values of Ra, Ha, and Re for Case 2 when $\lambda = 0°$

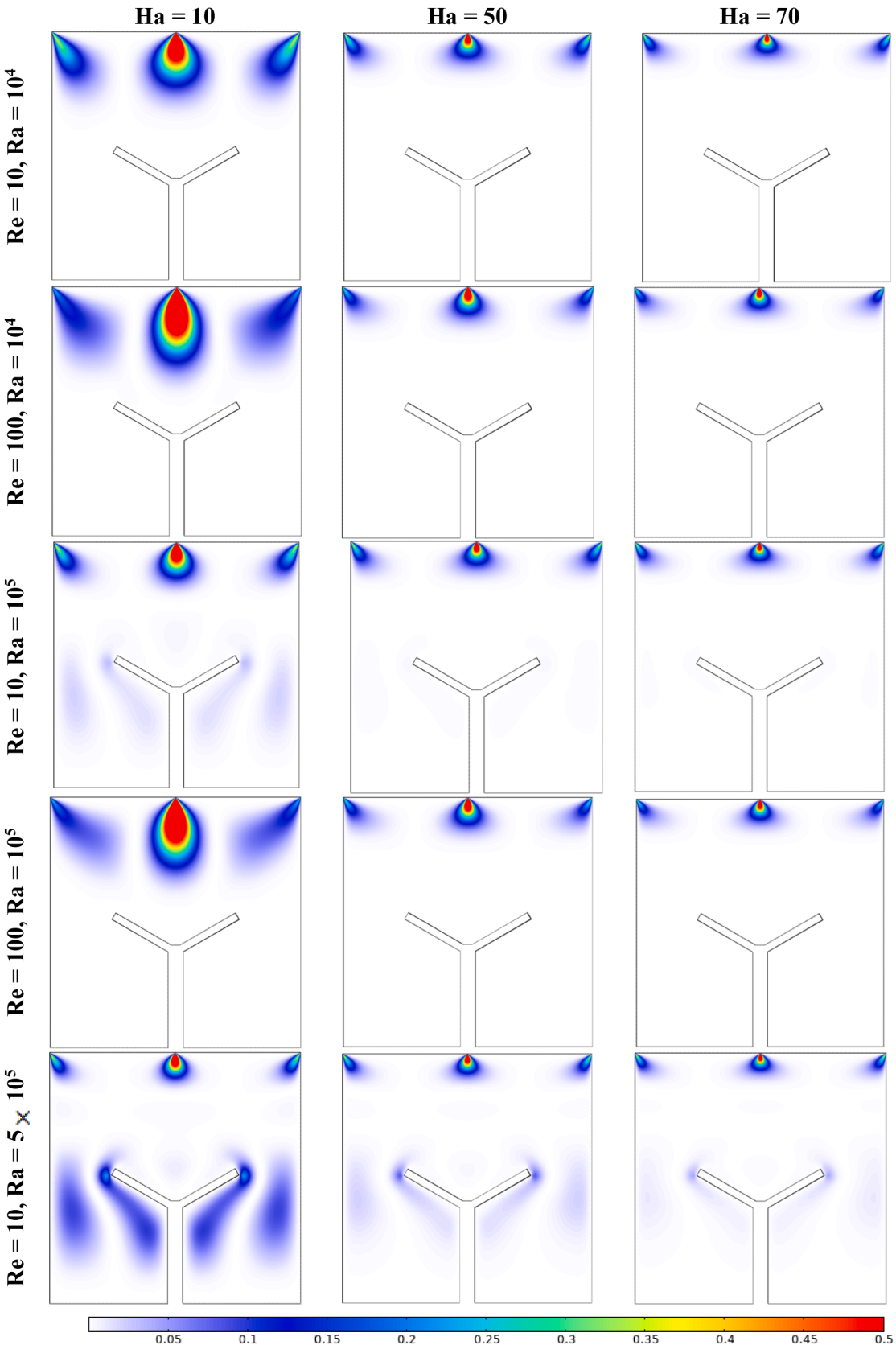

Fig. 14. Local contour plots for magnetic irreversibility, taking deferent values of Ra, Ha, and Re for Case 1 when $\lambda = 0^{\circ}$

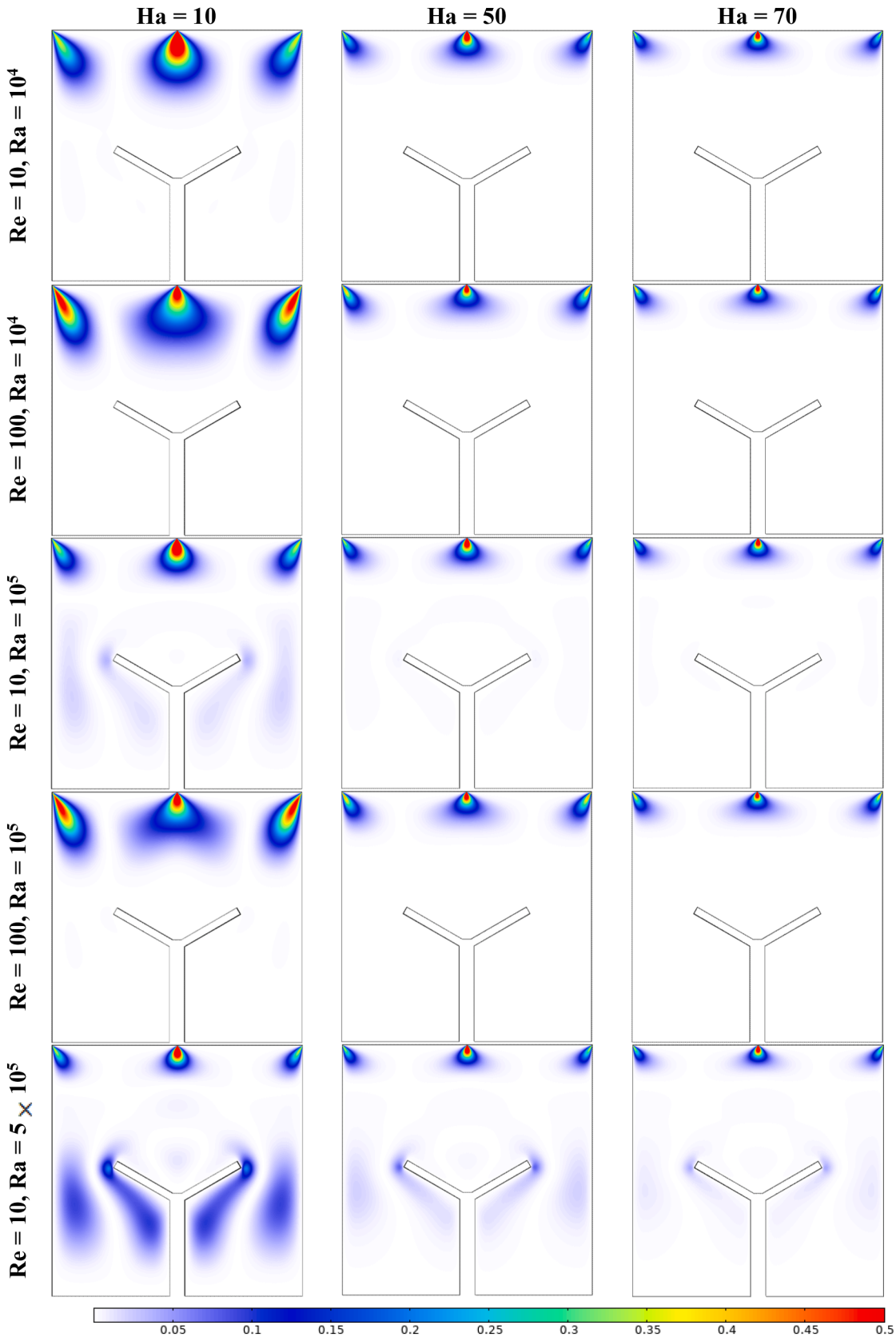

Fig. 15. Local contour plots for magnetic irreversibility, taking deferent values of Ra, Ha, and Re for Case 2 when $\lambda = 0^{\circ}$

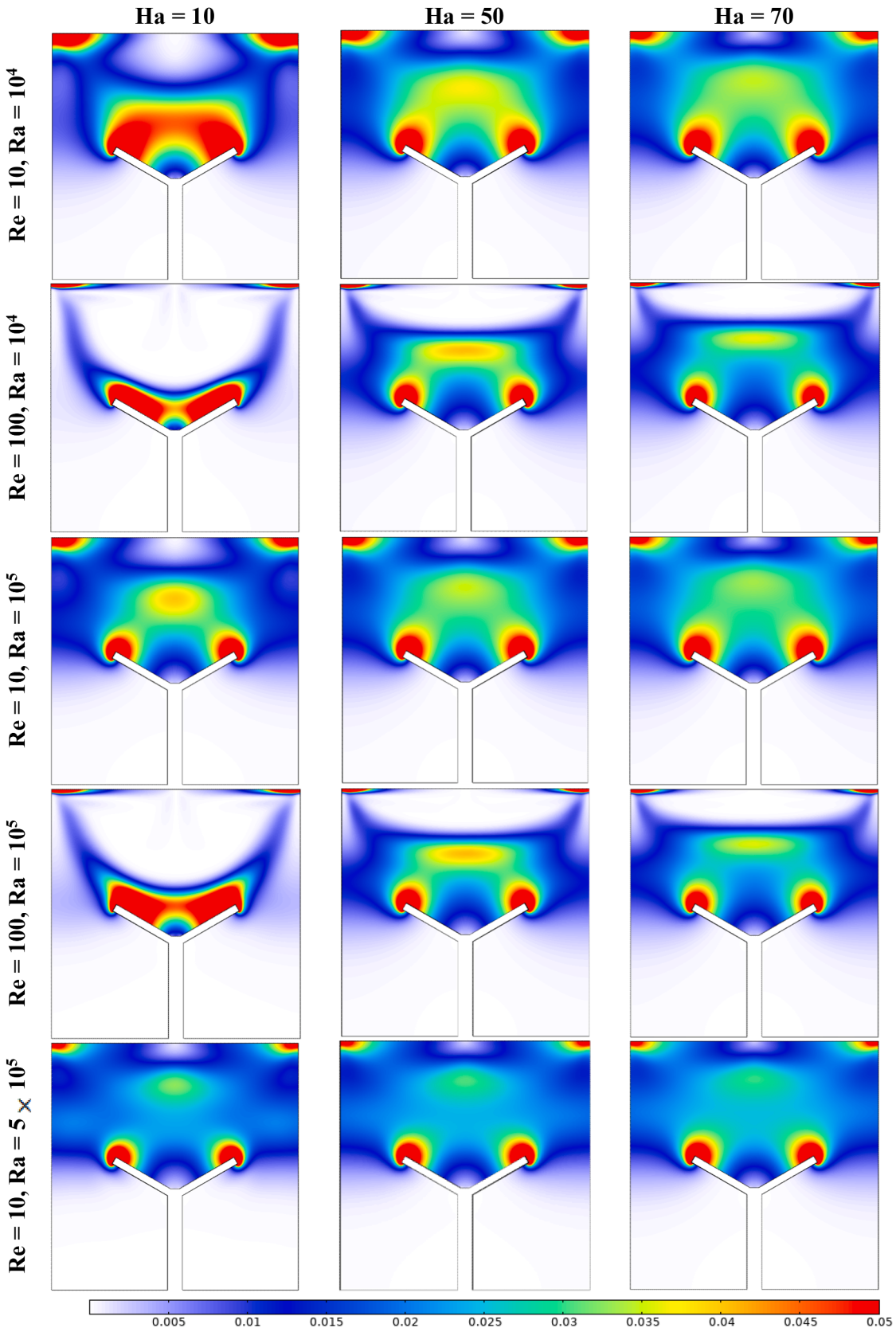

Fig. 16. Local contour plots for total irreversibility, taking deferent values of Ra, Ha, and Re for Case 1 when $\lambda = 0^{\circ}$

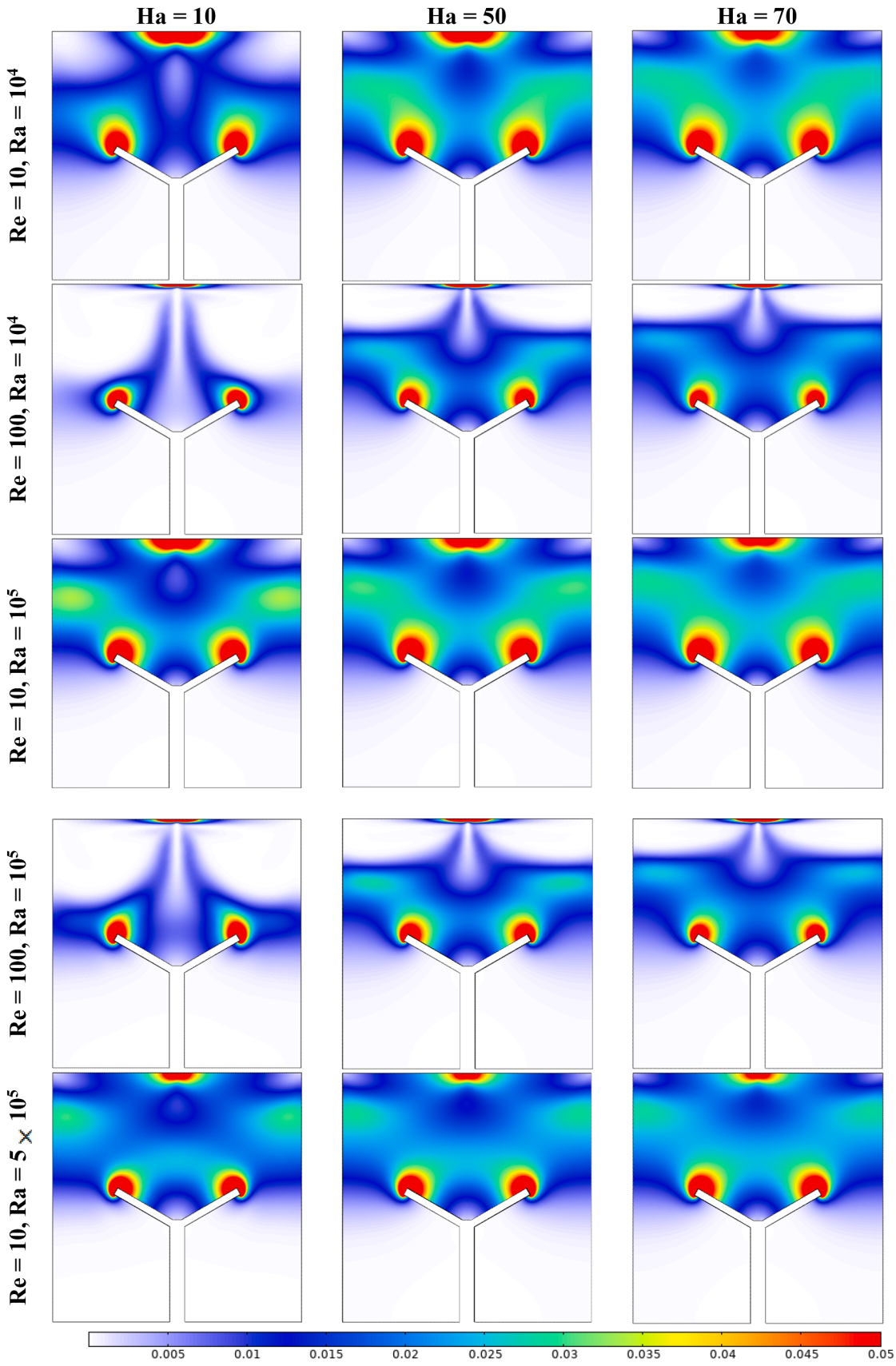

Fig. 17. Local contour plots for total irreversibility, taking deferent values of Ra, Ha, and Re for Case 2 when $\lambda = 0^{\circ}$

Table 5
Selected summary of outcome results through Nu, $|\psi_{max}|$, NS_v, NS_m, NS_{th}, and NS_{tot} for Case 1 ($U_l = +1$ and $U_r = -1$).

Re	Ra	Ha	λ	Nu	$\lvert\psi_{max}\rvert$	NS_v	NS_m	NS_{th}	NS_{tot}
10	10^3	0	–	2.831	0.056	2.47×10^{-11}	0	0.0257	0.0257
10	10^3	30	30	2.203	0.036	2.63×10^{-11}	3.53×10^{-12}	0.0200	0.0200
10	10^3	30	75	2.279	0.029	2.71×10^{-11}	6.85×10^{-12}	0.0207	0.0207
10	10^3	70	30	1.992	0.022	3.06×10^{-11}	9.24×10^{-12}	0.0181	0.0181
10	10^3	70	75	2.022	0.014	3.55×10^{-11}	1.84×10^{-11}	0.0184	0.0184
10	10^5	0	–	2.068	0.033	1.25×10^{-12}	0	0.0188	0.0188
10	10^5	30	30	2.016	0.028	1.28×10^{-12}	1.41×10^{-13}	0.0183	0.0183
10	10^5	30	75	2.028	0.023	1.33×10^{-12}	2.91×10^{-13}	0.0184	0.0184
10	10^5	70	30	1.959	0.020	1.45×10^{-12}	4.16×10^{-13}	0.0178	0.0178
10	10^5	70	75	1.983	0.013	1.68×10^{-12}	8.34×10^{-13}	0.0180	0.0180
100	10^3	0	–	8.021	0.064	2.57×10^{-11}	0	0.0730	0.0730
100	10^3	30	30	4.907	0.036	2.64×10^{-11}	3.74×10^{-12}	0.0447	0.0447
100	10^3	30	75	6.466	0.030	2.73×10^{-11}	6.91×10^{-12}	0.0588	0.0588
100	10^3	70	30	3.742	0.022	3.06×10^{-11}	9.31×10^{-12}	0.0341	0.0341
100	10^3	70	75	5.273	0.014	3.56×10^{-11}	1.84×10^{-11}	0.0480	0.0480
100	10^5	0	–	6.607	0.059	1.19×10^{-12}	0	0.0601	0.0601
100	10^5	30	30	3.993	0.034	1.23×10^{-12}	1.66×10^{-13}	0.0363	0.0363
100	10^5	30	75	5.196	0.029	1.28×10^{-12}	3.12×10^{-13}	0.0473	0.0473
100	10^5	70	30	3.378	0.022	1.43×10^{-12}	4.27×10^{-13}	0.0307	0.0307
100	10^5	70	75	4.577	0.014	1.66×10^{-12}	8.46×10^{-13}	0.0417	0.0417
200	10^3	0	–	12.468	0.069	2.76×10^{-11}	0	0.1136	0.1136
200	10^3	30	30	6.810	0.036	2.69×10^{-11}	4.13×10^{-12}	0.0620	0.0621
200	10^3	30	75	9.197	0.032	2.79×10^{-11}	6.95×10^{-12}	0.0838	0.0838
200	10^3	70	30	4.865	0.022	3.07×10^{-11}	9.44×10^{-12}	0.0443	0.0443
200	10^3	70	75	7.667	0.014	3.57×10^{-11}	1.84×10^{-11}	0.0699	0.0699
200	10^5	0	–	11.927	0.067	1.28×10^{-12}	0	0.1087	0.1087
200	10^5	30	30	6.028	0.036	1.25×10^{-12}	1.87×10^{-13}	0.0550	0.0550
200	10^5	30	75	8.481	0.031	1.30×10^{-12}	3.18×10^{-13}	0.0773	0.0773
200	10^5	70	30	4.554	0.022	1.43×10^{-12}	4.35×10^{-13}	0.0415	0.0415
200	10^5	70	75	7.103	0.014	1.66×10^{-12}	8.52×10^{-13}	0.0648	0.0648

Table 6
Selected summary of outcome results through Nu, $|\psi_{max}|$, NS_v, NS_m, NS_{th}, and NS_{tot} for Case 2 ($U_l = -1$ and $U_r = +1$).

Re	Ra	Ha	λ	Nu	$\lvert\psi_{max}\rvert$	NS_v	NS_m	NS_{th}	NS_{tot}
10	10^3	0	–	2.790	0.055	2.47×10^{-11}	0	0.0254	0.0254
10	10^3	30	30	2.198	0.032	2.63×10^{-11}	3.50×10^{-12}	0.0200	0.0200
10	10^3	30	75	2.271	0.028	2.71×10^{-11}	6.84×10^{-12}	0.0206	0.0206
10	10^3	70	30	1.992	0.019	3.06×10^{-11}	9.23×10^{-12}	0.0181	0.0181
10	10^3	70	75	2.021	0.014	3.55×10^{-11}	1.84×10^{-11}	0.0184	0.0184
10	10^5	0	–	2.055	0.033	1.26×10^{-12}	0	0.0187	0.0187
10	10^5	30	30	2.005	0.027	1.29×10^{-12}	1.40×10^{-13}	0.0182	0.0182
10	10^5	30	75	2.001	0.022	1.34×10^{-12}	2.96×10^{-13}	0.0182	0.0182
10	10^5	70	30	1.959	0.018	1.45×10^{-12}	4.12×10^{-13}	0.0178	0.0178
10	10^5	70	75	1.957	0.013	1.69×10^{-12}	8.40×10^{-13}	0.0178	0.0178
100	10^3	0	–	6.202	0.055	2.54×10^{-11}	0	0.0564	0.0564
100	10^3	30	30	4.512	0.031	2.67×10^{-11}	3.42×10^{-12}	0.0410	0.0410
100	10^3	30	75	6.068	0.028	2.74×10^{-11}	6.78×10^{-12}	0.0552	0.0552
100	10^3	70	30	3.658	0.019	3.07×10^{-11}	9.17×10^{-12}	0.0333	0.0333
100	10^3	70	75	5.208	0.014	3.56×10^{-11}	1.84×10^{-11}	0.0474	0.0474
100	10^5	0	–	4.771	0.050	1.19×10^{-12}	0	0.0434	0.0434
100	10^5	30	30	3.809	0.031	1.25×10^{-12}	1.54×10^{-13}	0.0346	0.0346
100	10^5	30	75	4.614	0.027	1.29×10^{-12}	3.08×10^{-13}	0.0420	0.0420
100	10^5	70	30	3.433	0.019	1.43×10^{-12}	4.22×10^{-13}	0.0312	0.0312
100	10^5	70	75	4.255	0.013	1.66×10^{-12}	8.44×10^{-13}	0.0387	0.0387
200	10^3	0	–	7.723	0.056	2.68×10^{-11}	0	0.0703	0.0703
200	10^3	30	30	5.507	0.031	2.74×10^{-11}	3.40×10^{-12}	0.0501	0.0501
200	10^3	30	75	7.940	0.028	2.80×10^{-11}	6.69×10^{-12}	0.0722	0.0722
200	10^3	70	30	4.632	0.019	3.10×10^{-11}	9.14×10^{-12}	0.0421	0.0421
200	10^3	70	75	7.495	0.014	3.58×10^{-11}	1.83×10^{-11}	0.0682	0.0682
200	10^5	0	–	7.037	0.054	1.25×10^{-12}	0	0.0640	0.0640
200	10^5	30	30	4.960	0.031	1.27×10^{-12}	1.56×10^{-13}	0.0451	0.0451
200	10^5	30	75	6.793	0.028	1.30×10^{-12}	3.07×10^{-13}	0.0618	0.0618
200	10^5	70	30	4.461	0.019	1.44×10^{-12}	4.23×10^{-13}	0.0406	0.0406
200	10^5	70	75	6.479	0.014	1.67×10^{-12}	8.47×10^{-13}	0.0590	0.0590

5. Conclusions

This study provides valuable insights into the complex behavior of MHD mixed convection in a nanofluid-filled split lid-driven cavity with a Y-shaped obstacle. The effects of key parameters such as Reynolds number (Re), Rayleigh number (Ra), Hartmann number (Ha), and magnetic field inclination (λ) on flow dynamics, heat transfer, and entropy generation were systematically investigated. Key findings include:

1. **Novel geometry**: The split lid-driven cavity with a Y-shaped obstacle creates unique flow patterns and heat transfer characteristics not adequately explored in literature. Case 1 (inward translation) is generally optimal for $\lambda = 0°$, while Case 2 (outward translation) can be more effective for certain parameter ranges across the λ space.
2. **Comprehensive parameter analysis**: Examination of a wide range of Re, Ra, Ha, and λ values has mapped the system's behavior across various operating conditions, providing a thorough understanding of the complex interactions at play.
3. **Practical implications**: The results directly inform the design of thermal management systems, particularly for applications requiring compact, high-performance heat transfer solutions in industries such as electronics cooling, metal casting processes, and HVAC systems.
4. **Optimization potential**: Optimal conditions (e.g., Re = 200, Ra = 10^5, Ha = 0, $\lambda \approx 75°$) provide clear targets for maximizing heat transfer efficiency in similar systems.
5. **Entropy generation analysis**: Consideration of both heat transfer and irreversibilities provides a more complete picture of system performance, enabling more informed design decisions.

Key evidence supporting these conclusions includes a 65 % increase

in Nusselt number with increasing Re, a non-monotonic relationship between Ra and heat transfer, significant impacts of magnetic field characteristics on flow patterns, and a 30 % local heat transfer enhancement near the Y-shaped obstacle. These findings demonstrate the complex interplay of forced convection, buoyancy forces, MHD effects, and geometric factors in optimizing system performance.

The study demonstrates that careful optimization of flow parameters, magnetic field characteristics, and geometric features can enhance heat transfer efficiency while minimizing entropy generation. However, practical implementation must consider trade-offs between enhanced heat transfer and increased power requirements for split-lid translations. Future research could explore different obstacle geometries, transient conditions, and nanofluid compositions to further advance high-performance thermal management systems across diverse industrial applications.

CRediT authorship contribution statement

Anurag Kabiraj: Writing – original draft, Resources, Methodology, Investigation, Formal analysis. **Nirmalendu Biswas:** Writing – review & editing, Visualization, Validation, Investigation, Formal analysis, Conceptualization. **Nirmal K. Manna:** Writing – review & editing, Visualization, Software, Methodology, Data curation, Conceptualization. **Dipak Kumar Mandal:** Visualization, Supervision, Resources, Formal analysis. **Ali J. Chamkha:** Visualization, Supervision, Software, Resources.

Declaration of competing interest

The authors declare that they have no known competing financial interests or personal relationships that could have appeared to influence the work reported in this paper.

Data availability

Data will be made available on request.

References

[1] C.H. Bruneau, M. Saad, The 2D lid – driven cavity problem revisited, Comput. Fluids 35 (2006) 326–348.
[2] G. de Vahl Davis, Natural convection of air in a square cavity a bench mark numerical solution, Int. J. Numer. Methods Fluids 3 (1983) 249–264.
[3] M.K. Das, K.S.K. Reddy, Conjugate natural convection heat transfer in an inclined square cavity containing a conducting block, Int. J. Heat Mass Transf. 49 (2006) 4987–5000.
[4] S.M. Aminossadati, B. Ghasemi, Conjugate natural convection in an inclined nanofluid–filled enclosure, Int. J. Numer. Methods Heat Fluid Flow 22 (4) (2012) 403–423.
[5] A.A. Merrikh, J.L. Lage, Natural convection in an enclosure with disconnected and conducting solid blocks, Int. J. Heat Mass Transf. 48 (2005) 1361–1372.
[6] J.T. Hu, X.H. Ren, Di Liu, F.Y. Zhao, H.Q. Wang, Conjugate natural convection inside a vertical enclosure with solid obstacles of unique volume and multiple morphologies, Int. J. Heat Mass Transf. 95 (2016) 1096–1114.
[7] R. Mohebbi, M.M. Rashidi, Numerical simulation of natural convection heat transfer of a nanofluid in an L -shaped enclosure with a heating obstacle, J. Taiwan Inst. Chem. Eng. (2017) 1–15.
[8] N.Z. Khan, R. Mahmood, S. Bilal, A. Akgül, S. Abdullaev, E.E. Mahmoud, I.S. Yahia, C. Park, Mixed convective thermal transport in a lid–driven square enclosure with square obstacle, Alex. Eng. J. 64 (2023) 981–998.
[9] A.W. Islam, M.A.R. Sharif, E.S. Carlson, Mixed convection in a lid driven square cavity with an isothermally heated square blockage inside, Int. J. Heat Mass Transf. 55 (2012) 5244–5255.
[10] Z. Boulahia, A. Wakif, R. Sehaqui, Natural Convection heat transfer of the nanofluids in a square enclosure with an inside cold obstacle, Int. J. Innov. Sci. Res. 21 (2) (2016) 367–375.
[11] G.C. Bourantas, V.C. Loukopoulos, MHD natural – convection flow in an inclined square enclosure filled with a micropolar – nanofluid, Int. J. Heat Mass Transf. 79 (2014) 930–944.
[12] T. Javed, M.A. Siddiqui, Effect of MHD on heat transfer through ferrofluid inside a square cavity containing obstacle/heat source, Int. J. Therm. Sci. 125 (2018) 419–427.
[13] T. Javed, M.A. Siddiqui, Energy transfer through mixed convection within square enclosure containing micropolar fluid with non–uniformly heated bottom wall under the MHD impact, J. Mol. Liq. 249 (2018) 831–842.
[14] M.M. Ali, M.A. Alim, M.A. Maleque, S.S. Ahmed, Numerical simulation of MHD free convection flow in a differentially heated square enclosure with tilted obstacle, AIP Conf. Proc. 1851 (2017) 020055.
[15] A.K. Hussein, H.R. Ashorynejad, S. Sivasankaran, L. Kolsi, M. Shikholeslami, I. K. Adegun, Modelling of MHD natural convection in a square enclosure having an adiabatic square shaped body using lattice boltzmann method, Alex. Eng. J. 55 (2016) 203–214.
[16] S. Parvin, R. Nasrin, Analysis of the flow and heat transfer characteristics for MHD free convection in an enclosure with a heated obstacle, Nonlinear Anal. Model. Control 16 (1) (2011) 89–99.
[17] M. Usman, Z.H. Khan, M.B. Liu, MHD natural convection and thermal control inside a cavity with obstacles under the radiation effects, Physica A 535 (2019) 122443.
[18] M. Ashouri, M. Behshad Shafii, H. Rajabi Kokande, MHD natural convection flow in cavities filled with square solid blocks, Int. J. Numer. Methods Heat Fluid Flow 24 (8) (2014) 1813–1830.
[19] Z.H. Khan, W.A. Khan, M. Hamid, Hongtao Liu, Finite element analysis of hybrid nanofluid flow and heat transfer in a split lid – driven square cavity with y – shaped obstacle, Phys. Fluids 32 (2020) 093609.
[20] N. Acharya, A.J. Chamkha, On the magnetohydrodynamic Al_2O_3-water nanofluid flow through parallel fins enclosed inside a partially heated hexagonal cavity, Int. Commun. Heat Mass Transf. 132 (2022) 105885.
[21] S. Izadi, T. Armaghani, R. Ghasemiasl, A.J. Chamkha, M. Molana, A comprehensive review on mixed convection of nanofluids in various shapes of enclosures, Powder Technol 343 (2019) 880–907.
[22] A. Kaggwa, J.K. Carson, Developments and future insights of using nanofluids for heat transfer enhancements in thermal systems: a review of recent literature, Int. Nano Lett. 9 (4) (2019) 277–288.
[23] L. Lukose, T. Basak, A comprehensive review on mixed convection for various patterns of kinematically and thermally induced scenarios within cavities, Int. J. Numer. Methods Heat Fluid Flow 31 (9) (2021) 2879–2939.
[24] T. Lemée, G. Kasperski, G. Labrosse, R. Narayanan, Multiple stable solutions in the 2D symmetrical two-sided square lid-driven cavity, Comput. Fluids 119 (2015) 204–212.
[25] N. Biswas, D.K. Mandal, N.K. Manna, Ali Cemal Benim, Magneto-hydrothermal triple-convection in a W-shaped porous cavity containing oxytactic bacteria, Sci. Rep. 12 (2022) 18053.
[26] A. Halder, A. Bhattacharya, N. Biswas, N.K. Manna, MHD nanofluidic mixed convection in a butterfly-shaped cavity, Sādhanā 49 (2024) 80.
[27] K. Al-Farhany, M.A. Alomari, N. Biswas, A. Laouer, A.M. Abed, W. Sridhar, Magnetohydrodynamic double-diffusive mixed convection in a curvilinear cavity filled with nanofluid and containing conducting fins, Int. Commun. Heat Mass Transf. 144 (2023) 106802.
[28] H.A. Jabbar, K.J. Alwan, D.M. Hachim, A. Al-Manea, R. Al-Rbaihat, A. Alahmer, Comparative assessment of thermal oils and water as working fluids in parabolic trough collectors for enhanced solar power generation, Eng. Res. Express 6 (3) (2024) 035514.
[29] Q.R. Al-Amir, H.K. Hamzah, F.H. Ali, M. Hatami, W. Al-Kouz, A. Al-Manea, R. Al-Rbaihat, A. Alahmer, Investigation of natural convection and entropy generation in a porous titled Z-staggered cavity saturated by TiO2-water nanofluid, Int. J. Thermofluids 19 (2023) 100395.
[30] D. Chatterjee, N. Biswas, N.K. Manna, D.K. Mandal, A.J. Chamkha, Magneto-nanofluid flow in cylinder-embedded discretely heated-cooled annular thermal systems: conjugate heat transfer and thermodynamic irreversibility, J. Magn. Magn. Mater. 569 (2023) 170442.
[31] P.S. Mahapatra, A. Mukhopadhyay, N.K. Manna, K. Ghosh, Heatlines and other visualization techniques for confined heat transfer systems, Int. J. Heat Mass Transf. 118 (2018) 1069–1079.
[32] S. Kimura, A. Bejan, The heatline visualization of convective heat transfer, J. Heat Transf. 105 (1983) 916–919.
[33] Z. Al-Dulaimi, H.T. Kadhim, M.F. Jaffer, A. Al-Manea, R. Al-Rbaihat, A. Alahmer, Enhanced conjugate natural convection in a corrugated porous enclosure with Ag-MgO hybrid nanofluid, Int. J. Thermofluids 21 (2024) 100574.
[34] S.Y. Ahmed, Q.R. Al-Amir, H.K. Hamzah, F.H. Ali, A.M. Abed, A. Al-Manea, K. Egab, R. Al-Rbaihat, K. Saleh, A. Alahmer, Investigation of natural convection and entropy generation of non-Newtonian flow in molten polymer-filled odd-shaped cavities using finite difference lattice Boltzmann method, Numer. Heat Transf. Part B Fundam. (2024) 1–26.
[35] A. Halder, A. Bhattacharya, N. Biswas, N.K. Manna, MHD nanofluidic mixed convection in a butterfly-shaped cavity, Sādhanā 49 (2024) 80.
[36] S. Pandit, M.K. Mondal, N.K. Manna, D. Sanyal, N. Biswas, D.K. Mandal, Synergistic effects of multi-segmented magnetic fields, wavy-segmented cooling, and distributed heating on hybrid nanofluid convective flow in tilted porous enclosures, Int. J. Thermofluids 24 (2024) 100826.
[37] D.K. Mandal, M.K. Mondal, N. Biswas, N.K. Manna, K. Al-Farhany, A. Mitra and A. J. Chamkha, Convective heat transport in a porous wavy enclosure: nonuniform multi-frequency heating with hybrid nanofluid and magnetic field, Heliyon, 10 (9) (2024) e29846.
[38] N.K. Manna, A. Saha, N. Biswas, K. Ghosh, Shape matters: convection and entropy generation in magneto-hydrodynamic nanofluid flow in constraint-based analogous annular thermal systems, Numer. Heat Transfer A (2024), https://doi.org/10.1080/10407782.2024.2347585.

[39] N.K. Manna, A. Saha, N. Biswas, K. Ghosh, Constraint-based analysis of heat transport and irreversibility in magnetic nanofluidic thermal systems, Int. J. Numer. Meth. Heat Fluid Flow (2024), https://doi.org/10.1108/HFF-06-2023-0329.
[40] N.K. Manna, N. Biswas, D.K. Mandal, C.K. Yadav, Steady and unsteady dynamics of magneto-nanofluidic flow in a bottom-heated top-cooled recto-triangular thermal system, Heat Transfer Engg 46 (4–5) (2024).
[41] A. Halder, A. Bhattacharya, N. Biswas, N.K. Manna, D.K. Mandal, Convective heat transport and entropy generation in butterfly-shaped magneto-nanofluidic systems with bottom heating and top cooling, Int. J. Numer. Meth. Heat Fluid Flow 34 (2) (2024) 837–877.
[42] B. Ghasemi, S.M. Aminossadati, A. Raisi, Magnetic field effect on natural convection in a nanofluid-filled square enclosure, Int. J. Therm. Sci. 50 (9) (2011) 1748–1756.
[43] M. Torki, N. Etesami, Experimental investigation of natural convection heat transfer of SiO_2/water nanofluid inside inclined enclosure, J. Therm. Anal. Calorim. 139 (2) (2020) 1565–1574.